Ligurian pyroxenite-peridotite sequences (Italy) and the role of melt-rock reaction in creating enriched-MORB mantle sources

Borghini, G. (1), Rampone, E. (2), Zanetti, A. (3), Class, C. (4), Fumagalli, P. (1), Godard, M. (5)

(1) Dip. Scienze Terra, University of Milano, via Botticelli 23, 20133 Milano, Italy
(2) DISTAV, Universiy of Genova, 16132 Genova, Italy
(3) CNR-IGG, Sez Pavia, via Ferrata 1, I-27100 Pavia, Italy
(4) Lamont Doherty Earth Observatory of Columbia University, 61 Route 9W, Palisades, NY 10964, USA
(5) Géosciences Montpellier, CNRS, Universite de Montpellier, Montpellier, France

Corresponding Author:

Elisabetta Rampone
Dipartimento di Scienze della Terra, dell'Ambiente e della Vita (DISTAV)
Università degli Studi di Genova
Corso Europa 26
I-16132 Genova (Italy)

Tel. 0039 10 3538315
Fax. 0039 10 352169
Email: betta@dipteris.unige.it

Keywords:

Pyroxenites, melt-rock reaction, Alpine-Apennine ophiolites, mantle peridotites, trace elements

Abstract

Deep melt intrusion and melt-peridotite interaction may introduce small-scale heterogeneity in the MORB mantle. These processes generate pyroxenite-bearing veined mantle that represent potential mantle sources of oceanic basalts. Natural proxies of such veined mantle are very rare and our understanding of mechanisms governing the chemical modification of mantle peridotite by MORB-type pyroxenite emplacement is very limited. We report the results of detailed spatially-controlled chemical profiles in pyroxenite-peridotite associations from the Northern Apennine ophiolitic mantle sequences (External Liguride Units, Italy), and investigate the extent and mechanism driving the local modification of peridotite by the interaction with pyroxenite-derived melt. Pyroxenites occur as cm-thick layers parallel to mantle tectonite foliation and show diffuse orthopyroxene-rich reaction rims along the pyroxenite-peridotite contact. Relative to distal unmodified peridotites, wall-rock peridotites show i) modal orthopyroxene enrichment at the expense of olivine, ii) higher Al, Ca, Si contents and slightly lower X_{Mg}, iii) Al-richer spinel and lower-X_{Mg} pyroxenes. Clinopyroxenes from wall-rock peridotites exhibit variable LREE-MREE fractionation, always resulting in Sm_N/Nd_N ratios lower than distal peridotites. From the contact with pyroxenite layers, peridotite clinopyroxenes record a REE compositional gradient up to about 15 cm marked by a overall REE increase away from the pyroxenite. Beyond 15 cm, and up to 23 cm, the MREE and HREE content decreases while the LREEs remain at nearly constant abundances. This REE gradient is well reproduced by a two-step numerical simulation of reactive melt percolation assuming variable amounts of olivine assimilation and pyroxene crystallization. Percolative reactive flow at decreasing melt mass and rather high instantaneous melt/peridotite ratio (initial porosity of 30%), combined with high extents of fractional crystallization (i.e. relatively low M_a/M_c ratio), accounts for the overall REE enrichment in the first 15 centimeters. Change of melt-rock reaction regime, mostly determined by the drastic decrease of porosity (Φ_i = 0.01) due to increasing crystallization rates, results in more efficient chemical buffering of the host peridotite on the HREE composition of the differentiated liquids through ion-exchange chromatographic-type processes, determining the observed increase of the LREE/HREE ratio. Emplacement of thin (cm-sized) pyroxenite veins by deep melt infiltration is able to metasomatize a much larger volume of the host peridotite. Hybrid mantle domains made by pyroxenite, metasomatized peridotite and unmodified peridotite potentially represent mantle sources of E-MORB. Results of this work stress the key role of melt-peridotite reactions in modifying the upwelling mantle prior to oceanic basalts production.

1. Introduction

Melt intrusion and melt-peridotite interaction are considered among the most efficient processes in creating small-scale heterogeneity in the upper mantle (e.g. Donnelly et al., 2004; Lambart et al., 2012; Mallik and Dasgupta, 2012). These processes can generate a pyroxenite-bearing veined mantle that is often invoked as a potential mantle source of oceanic basalts (e.g. Hirschmann and Stolper, 1996; Stracke et al., 1999; Sobolev et al., 2007; Herzberg, 2011; Shorttle and Mclennan, 2011; Lambart et al., 2013, 2016; Shorttle, 2014; Lambart, 2017).

Pyroxenites are believed to play a crucial role as the primary fertile component with relatively low melting temperatures in veined mantle sources. The origin of mantle pyroxenites can be related to a variety of magmatic and metamorphic processes, including recycling of subducted material (e.g. Allègre & Turcotte, 1986; Kornprobst et al., 1990; Morishita & Arai, 2001; Morishita et al., 2003; Yu et al., 2010; Varas-Reus et al., 2018), or high-pressure melt infiltration and/ or melt-rock reaction (e.g. Bodinier et al., 1987a,b; Rivalenti et al., 1995; Takazawa et al., 1999; Garrido & Bodinier, 1999; Mukasa & Shervais, 1999; Keshav et al., 2007; Bodinier et al., 2008; van Acken et al., 2010; Gysi et al., 2011; Borghini et al., 2016; Tilhac et al., 2016, 2017). Beyond their direct involvement in mantle partial melting processes, a crucial aspect of pyroxenite presence in mantle sources is the effect of the interaction between pyroxenite-derived melts and the surrounding mantle and how this process contributes to MORB chemical signatures by modifying the host peridotites.

To date, the few experimental studies, which have focused on high-pressure melt-peridotite reaction, have documented the formation of "hybrid" rocks as refertilized peridotites or secondary-type pyroxenites (e.g. Yaxley and Green, 1998; Lambart et al., 2012; Mallik and Dasgupta, 2012; Rosenthal et al., 2014; Yu et al., 2014; Wang et al., 2016). However, natural examples of such veined mantle are very rare and our understanding of mechanisms governing the chemical modification of mantle peridotite by pyroxenite emplacement at upper mantle levels is still limited. Indeed, despite of extensive literature on mantle metasomatism via melt percolation and melt-peridotite reaction (e.g. Godard et al., 1995, 2008; Ionov et al., 2002, 2005; le Roux et al., 2009; Brunelli et al., 2006, 2010, 2014; le Roex & Class, 2014; Kaczmarek et al., 2016; Mundl et al., 2016; Marchesi et al., 2017), few studies document mantle chemical modifications induced by and/or associated with pyroxenitic components (Bodinier et al., 1990, 2004; Pearson et al., 1993; Rivalenti et al., 1995; McPherson et al., 1996; Woodland et al., 1996; Varfalvy et al., 1996; Zanetti et al., 1996; Mukasa & Shervais, 1999).

Studies on lithospheric pyroxenite-peridotite associations in orogenic ultramafic massifs have provided important contributions on this issue, because they allow us to investigate the spatially-controlled chemical exchanges between mantle peridotites and pyroxenites. Systematic

investigations of some of these mantle outcrops have been based on centimeter- (rarely meter-) scale chemical profiles across veins and adjacent peridotite together with distal peridotite to investigate the effect of pyroxenite-peridotite interaction in terms of bulk-rock and mineral chemistry. They have shown that peridotites are locally modified in their modal and chemical composition by interaction with pyroxenite-derived melts (Bodinier et al., 1990, 2004; Pearson et al., 1993; Rivalenti et al., 1995; McPherson et al., 1996; Woodland et al., 1996; Varfalvy et al., 1996; Zanetti et al., 1996; Mukasa & Shervais, 1999; Ishimaru et al., 2017). Bodinier et al. (1990, 2004), in a detailed study of centimeter-scale aureoles around amphibole-bearing pyroxenite veins in the Lherz peridotite massif (France), documented significant elemental and isotopic heterogeneity resulting from interaction between peridotite and melt percolating from the adjacent vein, and they successfully applied geochemical models to simulate such metasomatic processes. However, metasomatism described in orogenic ultramafic massifs is usually related to infiltration of alkaline OIB-like melts, whereas the chemical modification of peridotite via interaction with MORB-type pyroxenite-derived melts has not yet been documented.

Mantle sequences from the Northern Apennines ophiolites (External Liguride Units, Italy) record an ancient (Ordovician) event of pyroxenite emplacement that modified cm-scale portions of the host peridotite producing trace element and Nd isotope enriched mantle domains (Borghini et al., 2013), and form a suitable source of E-MORB basalts (e.g. Salters and Dick, 2002). However, the underlying melt-rock reaction process between host peridotite and pyroxenite-derived melts still needs to be fully discerned.

In this paper, we report the results of detailed spatially-controlled chemical profiles 4 to 23 cm long through pyroxenite-peridotite boundaries in order to investigate to what extent the host peridotite is modified by local interaction with pyroxenite-derived melt. Through geochemical modelling we constrain the mechanisms driving reactive melt percolation and chemical exchange between melts and the peridotite mineral matrix. Results of this work are discussed in the context of our present knowledge on the origin of veined mantle sources.

2. Geological setting and petrological background

The Northern Apennine ophiolites represent remnants of the oceanic lithosphere of the Ligurian Tethys, a rather narrow oceanic basin developed by progressive divergence of Europa and Adria blocks related to the pre-Jurassic rifting and Middle Jurassic opening of the Northern Atlantic (Lemoine et al., 1987; Bill et al., 2001). They are considered as fossil analogue of present-day passive continental margins (e.g. the Iberian Margin) and ultra-slow-spreading ridges (e.g. the Gakkel and South West Indian ridges)(e.g. Rampone & Piccardo, 2000; Rampone et al., 1995,

2005, 2008, 2018; Müntener & Piccardo 2003; Müntener et al. 2004; Piccardo et al. 2004, 2007). The External Liguride ophiolites consist of several ultramafic bodies, with minor MOR-type basalts and rare gabbroic rocks, occurring as large olistoliths within Cretaceous sedimentary melanges obducted during the closure of the oceanic basin (e.g. Marroni et al., 2010).

Peridotite-pyroxenite associations have been documented in various ultramafic bodies outcropping in the External Liguride Units (Rampone et al., 1995; Montanini et al., 2006, 2012; Borghini et al., 2013, 2016; Montanini & Tribuzio, 2015). Mantle sequences investigated in this study are from three hundred-meter-sized peridotite slivers from the eastern sector of the External Liguride Units (Rampone et al., 1995; Borghini et al., 2013, 2106)(Supplementary Table 1). These ultramafic bodies consist of unaltered peridotites and dispersed pyroxenites preserving mantle textures and assemblages. In the peridotites, very depleted Sr, Nd isotopic compositions and lherzolitic chemical signature suggested that they were formed by lithospheric accretion of DM-type asthenospheric mantle since the Proterozoic (Rampone et al., 1995). Peridotites are mostly lherzolites with a well-developed foliation (Fig. 1a). Pyroxenites occur within the peridotites as cm-scale bands (from <1cm to 12-15 cm) parallel to the tectonite foliation plane of the host peridotites (Fig. 1b,c), with which they form sharp and boudinated contacts. They are variably distributed in the massifs and in places can constitute up to 50% of the outcrop (Borghini et al., 2013, 2016).

The origin and evolution of pyroxenites from the mantle outcrops studied in this work have been investigated by Borghini et al. (2016). Preserved trace element heterogeneity and garnet-like geochemical signature (i.e. high HREE contents and HREE/MREE fractionation) in clinopyroxene porphyroclasts indicate that most of the pyroxenites originally represented layers made by pyroxene and garnet. This is also indicated by HREE-enriched bulk-rock compositions shown by some pyroxenites and it has been supported by mass balance calculations (Borghini et al., 2016). The primary garnet-bearing mineral assemblage was completely replaced by the spinel-facies subsolidus recrystallization leading to the present spinel-bearing modes (Borghini et al., 2016). Consistently with the presence of garnet among the primary mineral association, pyroxenites have been interpreted as melt segregated into host spinel lherzolite at relatively high pressure (> 15 kbar, Borghini et al., 2016; Borghini & Fumagalli, 2018). Moreover, based on their bulk-rock chemical features, pyroxenites have been suggested to represent secondary-type pyroxenites originated from segregation of a tholeiitic low-MgO melt (X_{Mg} = 44-56) reacted to some extent with the host peridotite during mantle infiltration (Borghini et al., 2016).

Host peridotites have been modified in their modal, chemical and Nd isotopic compositions by reaction with melts derived from these secondary pyroxenite veins (Borghini et al., 2013). Chemical interaction between pyroxenite-derived melt and host peridotite generated along the

contact with pyroxenite layers aureoles of metasomatized peridotite having Rare Earth Element (REE)-enriched compositions. Moreover, Borghini et al. (2013) showed that variable enrichment of Nd over Sm in the host peridotites produced Nd isotopic heterogeneity over < 500 Ma that have greater range than observed in the peridotite and pyroxenite endmembers. Local Sm-Nd isochrons, defined by pyroxenite and adjacent wall-rock peridotite, in agreement with an errorchron of all the pyroxenites and reacted peridotites, indicate that pyroxenite emplacement occurred in Ordovician age (424-452 Ma, Borghini et al., 2013).

Subsequently, pyroxenite-peridotite associations experienced a rather cold decompressional tectonic evolution, related to the Jurassic opening of the Ligurian Tethys ocean, with both peridotites and pyroxenites partially affected by subsolidus spinel- to plagioclase-facies recrystallization (Borghini et al., 2011, 2016). As previously stated (Borghini et al., 2011, 2013, 2016), these pyroxenite-peridotite associations thus escaped melt-rock interaction and refertilization processes widely documented in mantle peridotites from oceanic (Niu, 2004 and references therein) and ophiolitic (e.g. Piccardo et al., 2004, 2007; Rampone et al., 1997, 2004, 2008; Rampone and Borghini 2008) settings, preserving the ancient chemical and isotopic variability acquired during melt infiltration and pyroxenitic melt-rock reaction at mantle depths. The origin and subsolidus evolution of the EL pyroxenites, as well as the Nd isotopic heterogeneity of the veined mantle resulted from their emplacement, have been subject of previous works (Borghini et al., 2013; Borghini et al., 2016). In this paper, we focus on the chemical modification of peridotite via interaction with pyroxenite-derived melts, and its implications on the origin of Enriched-MORB mantle sources.

3. Samples and analytical methods

In order to investigate the major and trace element chemical heterogeneity related to pyroxenite-peridotite interaction, we performed three cm-scale analytical profiles through the pyroxenite-peridotite boundary as follows: i) pyroxenite bands, which do not include the orthopyroxene-rich rims (Fig. 1c), ii) wall-rock peridotite (up to 4 cm from pyroxenite boundaries), iii) host peridotite (from 4 to 12 cm from pyroxenite boundaries)(Fig. 1c), and iv) country-rock peridotites sampled in pyroxenite-free outcrops (i.e. at least 2 m from pyroxenite bands, Fig. 1a). One pyroxenite-peridotite profile (GV8) for trace element analysis on clinopyroxene has been extended up to 23 cm from the pyroxenite-peridotite boundary.

Whole-rock major and trace elements of pyroxenites and peridotites (Table 1) were determined by lithium metaborate/tetraborate fusion ICP technique at the Actlabs Laboratories (Western Ontario, Canada). Trace elements (Sc, Ti, V, Sr, Y, Zr , La, Ce, Pr, Nd, Sm, Eu, Gd, Tb,

Dy, Ho, Er, Tm, Yb, Lu and Hf,) of some peridotite samples were were determined at Géosciences Montpellier (University de Montpellier, France) using an Agilent 7700X quadrupole ICP-MS. Powdered samples were prepared following the $HF/HClO_4$ procedure described in Ionov et al. (1992) and Godard et al. (2000). The samples were analysed after a dilution of 1000. Element concentrations were measured by external calibration, except for Nb and Ta that are calibrated by using Zr and Hf, respectively, as internal standards. This technique is an adaptation to ICP-MS analysis of the method described by Jochum et al. (1990) and aims at avoiding memory effects due to the introduction of concentrated Nb-Ta solutions in the instrument. The Helium cell gas mode of the Agilent 7700X was used to measure Sc, Ti, V, Co and Ni while removing polyatomic interferences. The external precision and accuracy of the analyses were assessed by measuring rock reference materials BIR-1 and UB-N as unknowns (Supplementary Table 2). Our results show good agreement between measured values and expected values for the international standards, and reproducibility is generally better than 1 % at concentrations > 1 µg/g; it is within 1-5% for concentrations of 10-1000 ng/g, and 5-10 % for concentrations less than 10 ng/g.

Mineral major element compositions were analyzed using: (1) a Philips SEM 515 equipped with an X-ray dispersive analyzer (accelerating potential 15 kV, beam current 20 nA), at the Dipartimento di Scienze della Terra, dell'Ambiente e della Vita, University of Genova, and (2) a JEOL JXA 8200 Superprobe equipped with five wavelength-dispersive (WDS) spectrometers, an energy dispersive (EDS) spectrometer, and a cathodoluminescence detector (accelerating potential 15 kV, beam current 15 nA), at the Dipartimento di Scienze della Terra, University of Milano.

In situ trace element analyses of individual mineral phases were carried out using laser ablation microprobe - inductively coupled plasma mass spectrometry (LAM-ICPMS) at IGG-CNR, Pavia (Italy). The laser probe consisted of a Q-switched Nd:YAG laser, model Quantel (Brilliant), whose fundamental emission in the near-IR region (1064 nm) was converted to 213 nm wavelength using three harmonic generators. The laser was operated at 10 Hz frequency, with a pulse energy of 35 mJ. Spot diameter was typically 50 µm. The ablated material was analyzed by using a PerkinElmer SCIEX ELAN DRC-e quadrupole mass spectrometer. Helium was used as carrier gas and mixed with Ar downstream of the ablation cell. NIST SRM 610 was used as external standard, while Ca was the internal standard for clinopyroxene. Data reduction was performed using the Glitter software. Precision and accuracy were assessed from repeated analyses of the BCR-2g reference material and resulted usually better than 10% (Supplementary Table 3).

4. Petrography

Peridotites are lherzolites characterized by porphyroclastic texture with a spinel-bearing

assemblage formed by porphyroclasts of pyroxenes, olivine and brown spinel partially substituted by a plagioclase-bearing granoblastic assemblage (Fig. 2a) developed along a fine-grained tectonite fabric (Rampone et al., 1995; Borghini et al., 2011). Modal abundances estimated by mass balance calculations indicated that the country-rock peridotites are spinel lherzolites (11-12% clinopyroxene, 24-27% orthopyroxene), whereas host and wall-rock peridotite have significantly higher modal orthopyroxene (33-39%) and lower olivine (45-52%) with slightly higher clinopyroxene amounts (12-14%) (Borghini et al., 2013).

Pyroxenites range from spinel-bearing clinopyroxenite to websterite showing mosaic equigranular to gneissic textures (Borghini et al., 2016). They are characterized by coarse mm-sized green spinel and pyroxene porphyroclasts partially replaced by a fine-grained plagioclase-bearing assemblage (Fig. 2b, see also Borghini et al., 2016). They typically display a systematic mineralogical zoning, parallel to the foliation, with pyroxene-rich and spinel-rich domains, the latter partially substituted by plagioclase and olivine (see Borghini et al., 2016).

Thin (> 2cm) irregular orthopyroxene-rich borders along pyroxenite-peridotite contact (Fig. 2c) indicate interaction between pyroxenite bands and host peridotites. Further evidence of interaction is represented by the occurrence of large blebs of orthopyroxene and hunter-green spinel in the wall-rock peridotites (Fig. 2d,e), generally observed up to 4 cm from the pyroxenite-peridotite boundary.

5. Whole-rock chemistry

Chemical profiles through pyroxenite-peridotite boundaries revealed that peridotites hosting pyroxenites are variably modified in their major and trace element compositions compared to the pyroxenite-free "country-rock peridotites". Both wall-rock and host peridotites display higher SiO_2, Al_2O_3 and CaO contents and lower X_{Mg} [molar $Mg/(Mg+Fe^{2+}_{tot})$] relative to the country-rock peridotites; pyroxenites show significantly higher Al_2O_3 and CaO contents and lower X_{Mg} than all the peridotites (Fig. 3a,b,c). Also, wall-rock and host peridotites are characterized by slightly higher TiO_2 contents with respect to the country-rock peridotites (Table 1).

Whole-rock trace element compositions of pyroxenites are highly variable in terms of LREE to HREE fractionation. This feature has been interpreted to reflect different abundances of primary phases (garnet and pyroxenes; Borghini et al., 2016). Figure 4 displays representative REE profiles of wall-rock and host peridotite compared to a representative country-rock peridotite. The latter exhibits a LREE depletion (Ce_N/Sm_N = 0.366-0.514) and nearly flat MREE-HREE at about 2 × CI (Fig. 4). BG8, BG14 and BG22 wall-rock peridotites are characterized by absolute REE concentrations slightly higher than the country-rock pyroxenites (Fig. 4). Although their REE

patterns mimic those of country-rock peridotites, they have moderately lower Sm_N/Nd_N ratios (wall-rock Sm_N/Nd_N = 1.16-1.21; country-rock peridotite Sm_N/Nd_N = 1.31-1.41) (Fig. 4). In the profile GV8, the wall-rock peridotite is relatively enriched in LREE, and slightly in MREE (Ce_N/Sm_N = 0.887), with respect to the country-rock peridotites (Ce_N/Sm_N = 0.37-0.51), resulting in an almost flat LREE-MREE pattern (Fig. 4). The associated host peridotite displays a similar REE pattern at higher absolute concentrations (Fig. 4), indicating that the peridotite is modified at least up to 12 cm from the contact with the pyroxenite band. The modified peridotites along profile GV8 have much lower Sm_N/Nd_N ratios (Sm_N/Nd_N = 0.93) relative to the country-rock peridotite (Fig. 4).

6. Mineral chemistry

Variations of major element composition in minerals along the selected pyroxenite-peridotite profiles are well evidenced by clinopyroxene and spinel (Supplementary Tables 4 and 5). Clinopyroxene porphyroclasts in pyroxenite layers are characterized by lower X_{Mg} and Cr contents (0.82-0.86 and 0.002-0.010 atoms per formula unit, a.p.f.u., respectively), and higher Al content (0.318-0.463 a.p.f.u.) with respect to distal country-rock peridotites (X_{Mg} = 0.89-0.91, Cr = 0.022-0.033 a.p.f.u., Al = 0.303-0.338 a.p.f.u.)(Fig. 5a,b). Clinopyroxene porphyroclasts in wall-rock and host peridotites show intermediate compositions of X_{Mg} (0.87-0.89) and Cr (0.014-0.027 a.p.f.u.), and Al (0.290-0.382 a.p.f.u.) concentrations partly overlapping those of clinopyroxene in country-rock peridotites (Fig. 5a,b). Similar chemical trends have been observed in orthopyroxenes (Supplementary Table 6). Brown spinels in country-rock peridotites display X_{Mg} varying from 0.73 to 0.76 and X_{Cr} [molar Cr/(Cr + Al)] within the range 0.12-0.19 (Fig. 5c). Green spinels in pyroxenite layers have X_{Mg} showing lower values 0.65-0.74, and significantly lower X_{Cr} (0.01-0.04)(Fig. 5c). Relative to spinels in the country-rock peridotites, hunter-green spinels in wall-rock peridotites exhibit similar X_{Cr} (0.11-0.18) coupled to lower X_{Mg} values (0.68-0.72) (Fig. 5c).

In-situ trace element analyses have been focused on spinel-facies clinopyroxene porphyroclasts (Table 2 and Supplementary Table 7). In order to avoid the trace element changes induced in clinopyroxene by partial plagioclase-bearing recrystallization affecting all the samples, we filtered laser ablation data by discarding trace element clinopyroxene compositions indicating re-equilibration with plagioclase (Supplementary Table 8). As documented by Rampone et al. (1993), plagioclase-bearing metamorphic recrystallization causes the development of negative anomalies in Sr and Eu in clinopyroxene, combined with relative HFSE and REE enrichment. Accordingly, besides careful petrographic observation, we filtered the data by excluding trace element analyses of clinopyroxene porphyroclasts showing Eu negative anomaly and low Sr coupled to relatively higher Zr, V and Sc concentrations.

Clinopyroxene porphyroclasts of pyroxenite layers display heterogeneous trace element composition in the different samples, in agreement with the trace element bulk-rock variability (Borghini et al., 2016). Also, they show variable MREE-HREE fractionation within a single sample likely reflecting the occurrence of precursor garnet in the primary assemblage (Borghini et al., 2016). In particular, markedly positive HREE slopes (Sm_N/Yb_N = 0.30-0.96) coupled with high Zr and Sc contents observed in some spinel-facies clinopyroxene indicate that they inherited the REE signature from a precursor garnet (Borghini et al., 2016).

In the profiles selected for this study, clinopyroxenes from pyroxenites BG14 and BG22 have flat to HREE enriched patterns (Sm_N/Yb_N=0.57-1.03) and LREE depletion (Ce_N/Sm_N = 0.34-0.50)(Fig. 6a,b), whereas in pyroxenite GV8 they are characterized by rather flat REE patterns, only slightly depleted in LREE (Ce_N/Sm_N = 0.59-0.77)(Fig. 6d). Negative Zr, Hf and Ti anomalies are always observed (Fig. 6).

In all three traverses, clinopyroxene porphyroclasts analysed within the first centimetres of the wall-rock peridotite have Zr, Hf, Ti, REE patterns significantly different from those of clinopyroxenes in the country-rock peridotites (Fig. 6a,b,c). Country-rock peridotites display constant LREE-MREE depletion (Ce_N/Sm_N = 0.37-0.54), rather flat MREE/HREE abundances (Sm_N/Yb_N = 0.88-1.17), and negative anomalies in Zr, Hf and Ti (Fig. 6a,b,c). By contrast, clinopyroxenes from wall-rock peridotites exhibit MREE-HREE fractionation (Sm_N/Yb_N = 1.23-1.79) coupled to variable LREE-MREE fractionation, from rather flat (Ce_N/Sm_N = 0.81-1.03) in the GV8 peridotites (Fig. 6c), to variably depleted (Ce_N/Sm_N = 0.49-0.63) in BG14 and BG22 wall-rocks (Fig. 6a,b). As discussed in Borghini et al. (2013), this likely reflects reactive percolation of melt from the pyroxenite conduit into the wall rock with decreasing melt mass with increasing distance from the boundary. Modified clinopyroxenes in wall-rock peridotites, in spite of variable LREE abundances, always show lower Sm_N/Nd_N ratios with respect to the country-rock peridotites (Fig. 6a,b,c). Consistent with observations in the bulk-rock compositions (see Fig. 4), REE abundances in clinopyroxene progressively increase with increasing distance from the pyroxenite-peridotite boundary. This chemical gradient is perpendicular to the pyroxenite-peridotite boundary, as evidenced by profiles BG14 and GV8 (Fig. 6a,c). The longest profile, GV8, shows that this homogenous REE increase persists up to about 15 centimetres from the pyroxenite vein (Fig. 6c). Beyond 15 cm, and up to 23 cm, the MREE and HREE content decreases while the LREEs remain at nearly constant abundances (Fig. 6d), and this results in a progressive La_N/Yb_N increase, from 0.39 to 0.73. Moreover, Sm_N/Nd_N ratios lower than those of country-rock peridotites are observed in wall-rock and host peridotite along the whole profile up to 23 cm from pyroxenite vein (Suppl. Fig. 1).

In all pyroxenite-peridotite profiles, clinopyroxenes preserve the negative Zr and Hf anomalies typical of these minerals (Rampone et al., 1991). Noteworthy, the negative Ti anomalies that characterize the composition of country-rock peridotites tends to decrease within the wall-rock peridotites suggesting a redistribution of this element between the peridotite constitutive phases at the contact with the pyroxenite layer (Fig. 6a,b,c).

7. Discussion

7.1 Mantle metasomatism via peridotite-pyroxenite derived melt interactions

Evidence of interaction between pyroxenite veins and host peridotite has often been described in ophiolitic and orogenic massifs (Bodinier et al., 1990, 2004; Pearson et al., 1993; Rivalenti et al., 1995; Varfalvy et al., 1996; Zanetti et al., 1996; McPherson et al., 1996; Mukasa & Shervais, 1999; Takazawa et al., 1999; Fabries et al., 2001). These studies have shown that pyroxenite intrusion at depth can lead to metasomatic reactions with mantle rocks resulting in modal and chemical changes in surrounding peridotites. The mineralogy of reacted peridotites depends on the composition of the infiltrating melt, pressure conditions and local proportion of melt added (Kogiso & Hirschmann, 2006). In thick mafic layers from Beni Boussera peridotite massif (North Morocco), the typical zonation sequence starting with garnet-clinopyroxenite at the center and orthopyroxenite to websterite at the periphery has been ascribed to the reaction between crystallizing melt and the host peridotite (Pearson et al., 1993). Orthopyroxenite-rich rims at the contact between mafic layers and host peridotites and enrichment of modal orthopyroxene in wall-rock peridotites have been described in orogenic (i.e. Takazawa et al., 1999; Fabries et al., 2001; Mazzucchelli et al., 2010) and ophiolitic (Varfalvy et al., 1996) mantle sequences. Modal changes are often coupled to Fe (and Al) and incompatible trace element enrichments with respect to the host peridotite far from the veins.

Mantle modification via melt-rock interaction has been investigated experimentally mostly for eclogite-derived melts (Yaxley & Green, 1998; Rapp et al., 1999, 2010; Sobolev et al., 2005; Mallik and Dasgupta, 2012; Wang et al., 2010; Wang et al., 2016). In particular, reaction between partial melts of silica-saturated pyroxenite and surrounding mantle is expected to increase the orthopyroxene mode and trace element fertility of the host peridotite (Yaxley & Green, 1998; Yaxley, 2000). Impregnation experiments have revealed the high silica activity of infiltrating melts leads to olivine dissolution and orthopyroxene precipitation during pyroxenite-peridotite interaction (Lambart et al., 2012).

Orthopyroxene-rich borders and orthopyroxene modal enrichment in the first centimeters of wall-rock peridotite observed in the studied pyroxenite-peridotite mantle association suggest that peridotites have been metasomatized by melt that was crystallizing the pyroxenites.

Critical issues in determining the nature and composition of pyroxenite parental melt are i) the subsolidus recrystallization that completely overprinted the primary garnet-bearing mineral assemblage, and ii) the melt-peridotite reaction, which occurred after melt infiltration and during the pyroxenite crystallization. Borghini et al. (2016) discussed the affinity of the parental melts and made some hypotheses on their mantle source. Based on microstructural and chemical observations, they concluded that pyroxenites originated from the segregation of low X_{Mg} and low alkali abundance typical of tholeiitic melts. The low X_{Mg} of these melts (44-56) could have been derived from chemical evolution requiring about 60% of fractional crystallization that is difficult to reconcile with the lack of magma chambers or intense fracturing at such depth in the mantle (e.g. Kelemen et al., 1995). As alternative hypothesis, Borghini et al. (2016) proposed that the X_{Mg}-evolved signature of infiltrating melt could have been produced by partial melting of a precursor mafic or pyroxenitic component or a mixed pyroxenite-peridotite source (in this case a silica-excess pyroxenite, Lambart et al., 2012). In particular, silica-saturated tholeiitic melts with relatively low X_{Mg} and alkali can result from reaction between eclogite-derived partial melts and fertile peridotite (Mallik and Dasgupta, 2012). Involvement of such melts well explains the development of orthopyroxene-rich lithologies resulting from the melt-peridotite reaction. Orthopyroxenite rims, as those observed along pyroxenite-peridotite boundaries (Fig. 2c), have been observed in experiments of reaction between peridotite and siliceous melts (e.g. Yaxley & Green, 1998; Wang et al., 2013, 2016; Pinter et al., 2015; Borghini et al., 2017), and the orthopyroxene modal enrichment of the wall-rock peridotite (Fig. 2e) is consistent with the reaction experimentally defined by Lambart et al. (2012):

$$SiO_2\text{-saturated melt} + \text{olivine} \rightarrow \text{orthopyroxene} \pm \text{clinopyroxene} \qquad (1)$$

Reaction (1) is in agreement with the mineral modes estimated for host and wall-rock peridotites, having significantly higher orthopyroxene and lower olivine contents compared to the country-rock peridotite (Borghini et al., 2013). Changes in modal mineralogy consistently reflect the bulk major element chemical modification observed in wall-rock and host peridotites, i.e. Si, Ca and Al content increase and Mg-number decrease relative to the country-rock peridotites (Fig. 3). Furthermore, changes in modal composition in proximity to the pyroxenites are coupled to major element chemical variations in minerals, namely X_{Cr} and X_{Mg} in spinel and X_{Mg} and Cr_2O_3 in

pyroxenes (Fig. 5), pointing to a percolating melt as the cause for those changes. Further supported by trace element gradients in bulk-rock and clinopyroxene chemical profiles (Fig. 4 and 6), these combined observations thus suggest that local peridotite modification in proximity to the pyroxenites was caused by reactive melt percolation (Borghini et al., 2013). Similar chemical trends have been documented in the first centimeters of peridotite hosting various types of pyroxenites in orogenic mantle massifs. In orogenic ultramafic massifs, pyroxenite veins emplacement mostly results from deep intrusion of variably hydrated alkaline melts, as documented in Lherz (e.g. Bodinier et al., 1990; MacPherson et al., 1996; Zanetti et al., 1996), and Balmuccia (e.g. Rivalenti et al., 1995; Mukasa & Shervais, 1999), or subduction-related magmas, as for Beni Boussera (e.g. Pearson et al., 1993; Pearson & Nowell, 2004; Gisy et al., 2011) and Ronda (e.g. Garrido & Bodinier, 1999; Bodinier et al., 2008; Marchesi et al., 2013). Distinctive chemical features of their wall-rock peridotites are the relatively low bulk X_{Mg} and Cr_2O_3 at higher Al_2O_3 contents (e.g. Bodinier et al., 1990; Shervais & Mukasa, 1991; Rivalenti et al., 1995), resulting from similar chemical changes in pyroxenes and spinel (e.g. Rivalenti et al., 1995; Mukasa & Shervais, 1999; Fabries et al., 2001; Bodinier et al., 2004). Consistent chemical variations are documented in wall-rock peridotite of pyroxenites generated by infiltration of basanitic melts (Varfalvy et al., 1996; Fabries et al., 2001).

In all cases, major element chemical modification related to the exchange with pyroxenite-derived melt is confined to the few first centimeters bordering the vein. Trace element cryptic metasomatism of host peridotite is sometimes more invasive (e.g. Menzies et al., 1987). Relatively long spatially-controlled chemical profiles on these pyroxenite-peridotite associations revealed that trace element modification of peridotite can occur over a distance of about 50 cm (MacPherson et al., 1996) or more than 1 meter (Bodinier et al., 1990). The distance of metasomatism is thought to be controlled by the volume of magma or metasomatic fluid available and, therefore, related to the thickness of the pyroxenite vein (Mukasa & Shervais, 1999).

The effects of mantle metasomatism (both major and trace elements) related to emplacement of amphibole-bearing pyroxenite veins have been studied in detail in the Lherz peridotite massif (Bodinier et al., 1990, 2004; Zanetti et al., 1996). These studies propose a geochemical model involving the combination of two mechanisms of metasomatism related to pyroxenite-peridotite interaction. Wall-rock peridotite in close proximity to the pyroxenite vein (<15-20 cm) is modally and chemically metasomatized by the chemical exchange with melt percolating by grain boundary flow from pyroxenite veins (diffusion-controlled silicate-melt metasomatism). At distance greater than 20 cm, chemical modification of host peridotites (e.g. enrichment of LREE relative to HREE) is driven by cryptic metasomatism (chromatographic effect: i.e. Bodinier et al., 1990). Bodinier et

al. (2004) demonstrated by numerical modeling that the elemental and isotopic heterogeneity in the Lherz wall-rock peridotites can be explained by a single stage of reactive porous flow.

Our study on mantle sequences from Northern Apennine ophiolites represents the first case study of the effect of pyroxenite-derived melt infiltration on host peridotite in a MORB-type mantle. Petrographic observations (orthopyroxene enrichment) and trace element chemical gradients along pyroxenite-peridotite traverses suggest that metasomatism of pyroxenite-bearing peridotite was dominated by re-equilibration of the peridotite minerals with a transient pyroxenite-related melt. To test this hypothesis, we modelled this reactive percolation process using parameters well constrained by our petrographic observations.

7.2 Mechanism of local mantle metasomatism: REE Modelling

To constrain the mechanism controlling the trace element variability related to reactive percolation of melts from pyroxenite layers through the adjacent peridotite, we performed a geochemical model using the "Plate Model" numerical simulation for the REEs of Vernières et al. (1997). This model reproduces a rock-dominated system where the solid matrix, varying in porosity and in modal composition along the percolation column, buffers the composition of the infiltrating melt. In our case, the mantle column consists of cm-scale portions ("cells") of peridotite that is penetrated by the same melts as those that formed the vein pyroxenites. Cell 1 is adjacent to the source of infiltrating melt, i.e. the pyroxenite layer, whereas cell 10 is furthest away. In our model, the nature and extent of the reactions varies along the column to simulate the changes in the melt reactivity resulting from melt-rock interactions. These parameters are constrained by petrographic and chemical observations in the pyroxenite-peridotite profiles.

We applied the Plate Model (Vernieres et al., 1997) to simulate changes in REE composition along profiles BG14 and GV8. The initial solid matrix, is a spinel lherzolite Ol:Opx:Cpx:Sp = 0.60:0.25:0.12:0.03 that is representative of the modal composition estimated for the studied country-rock peridotites (Borghini et al., 2013). REE compositions of the mineral phases olivine, orthopyroxene and spinel are assumed to be in equilibrium with the average REE composition of clinopyroxene porphyroclasts from country-rock peridotite GV18 (Table 1), calculated using partition coefficients by Ionov et al. (2002).

Regarding the choice of the reacting melt composition several points must be taken into account. As stated above, peridotites were metasomatized by the melt that was crystallizing the pyroxenites. Hence, in principle, we should use the trace element composition of clinopyroxene in the pyroxenites, to derive the composition of the infiltrating melt. However, Borghini et al. (2016) showed that the spinel-facies clinopyroxene porphyroclasts in the pyroxenites are not representative

of the trace element composition of primary (garnet-facies) clinopyroxene that crystallized from the parental melt. Rather, in most pyroxenites, clinopyroxene acquired a "garnet-like" chemical signature, due to close-system subsolidus recrystallization from garnet- to spinel-bearing mineral assemblage. For this reason, we obtained the REE composition of initial reacting melts by computing the liquids in equilibrium with wall-rock clinopyroxene immediately adjacent to the orthopyroxene-rim along the pyroxenite-peridotite contact. This approach is based on the evidence that the host lherzolite was at spinel-facies conditions during pyroxenite emplacement, hence spinel-facies clinopyroxene porphyroclasts crystallized at the contact with pyroxenite veins were not modified by subsolidus recrystallization and likely retained the trace element signature acquired by interaction with pyroxenite-derived melts (Borghini et al., 2013).

The REE patterns of clinopyroxene porphyroclasts and computed equilibrium liquids are shown in Figure 7a. The equilibrium melts have an LREE-enriched signature similar to E-MORB melts from modern mid-ocean-ridge settings (Borghini et al., 2016). Together with the relatively high-silica activity and low X_{Mg} (44-56), the E-MORB imprint of these melts have suggested their possible origin from a heterogeneous pyroxenite(or eclogite)-bearing mantle source (Borghini et al., 2016).

Reaction (1) that controls the modal metasomatism in the wall-rock peridotite is modeled by 100% olivine assimilation along the whole column, crystallization of 100% orthopyroxene close to the melt source and crystallization of (50% orthopyroxene - 50% clinopyroxene) far from this source. The crystallization of such pyroxene-rich pockets in the host peridotites, related to melt infiltration from the adjacent pyroxenites, have been revealed by Electron Backscattered Diffraction (EBSD) investigations on the pyroxenite-peridotite profiles (Hidas et al., in preparation). We also assumed a relatively high initial porosity (Φ_i) of 0.3 at the wall-rock peridotite / pyroxenite interface. This is consistent with the idea that the observed orthopyroxene-rich borders formed by the interaction between the infiltrating melt and the wall-rock peridotite concomitant with pyroxenite segregation. Formation of orthopyroxenite at the melt-peridotite interface has been observed in experiments of reaction between peridotite and both hydrous and anhydrous andesitic melts (Wang et al., 2013, 2016; Borghini et al., 2017). In particular, the crystallization of such pure orthopyroxene rim suggests the reaction with melts characterized by high silica combined to relatively low calcium contents (Wang et al., 2010). After orthopyroxene precipitation, the increase of CaO content of the residual infiltrating melt should favor the crystallization of clinopyroxene + orthopyroxene in the wall-rock peridotite, as shown by experiments of peridotite impregnation by pyroxenite-derived melts (Lambart et al., 2012).

Moreover, high melt/rock ratios have been proposed for the origin of abyssal pyroxenites from Lena Trough (Artic Ocean, Laukert et al., 2014), by reactive crystallization including assimilation of the host peridotite and fractional crystallization of the infiltrating melts. As reaction progresses and the reacting melt percolates the host peridotite matrix at increasing distance from the layer, the porosity is significantly reduced by the low M_a/M_c ratio (0.61) set for melt/rock reaction, i.e. the ratio between assimilated olivine (M_a) and crystallized pyroxenes mass (M_c). This is indicated by our petrographic observations on pyroxenite-peridotite profiles showing that the pyroxene modal enrichment (mostly opx) related to the melt-rock reaction is confined in the first centimeters of the infiltrated peridotite (i.e. the wall-rock peridotite).

The model has been applied to profiles BG14 and GV8 and the results in terms of REE concentrations of reacted clinoproxene are shown in Figure 7b,c and reported in Supplementary Table 9. The progressive increase of REE abundances in clinopyroxene of peridotites with increasing distance from pyroxenite veins is well reproduced by percolative reactive flow at decreasing melt mass, i.e. assuming relatively high initial melt/rock ratio combined with high extent of crystallization during percolation, at moderate mass assimilation. This REE gradient in clinopyroxene characterizes the wall-rock peridotite in profile BG14 (Fig. 7b) and the wall-rock and host peridotites up to about 15 cm in the longest profile GV8 (Fig. 7c). In profile GV8, the HREE decrease when LREE concentrations remain constant beyond 15 cm from the contact (Fig. 6d), suggesting a change in melt-rock reaction regime that we reproduce here through a *second step* of Plate Model simulation. In the *second step*, we assume the same percolated peridotite matrix but with a significantly lower initial porosity (Φ_i = 0.01). As starting reacting melt, we used the composition of liquid in equilibrium with computed clinopyroxene REE pattern of *cell 10*, i.e. the most REE-enriched clinopyroxene in the model of Figure 7c. Olivine is still the dissolving phase, initial and final crystallization have been fixed at 50% orthopyroxene and 50% clinopyroxene, according to petrographic observations (see above).

Model results closely match the REE gradient observed in the distal clinopyroxenes within the host peridotite (15-23 cm; Fig. 7d). At much lower melt-peridotite ratio and lower M_a/M_c ratio of about 0.8, the REE composition of clinopyroxenes modified by reactive melt percolation is more efficiently affected by chemical buffering of the host peridotite. This is indicated by the progressive decrease of M- and HREE towards the relative concentrations of clinopyroxene in the unmodified country-rock peridotite (Fig. 7d). This, in turn, leads to LREE/MREE fractionation that is typically documented in cryptically metasomatized clinopyroxenes in mantle peridotite and ascribed to ion-exchange chromatographic-type fractionation as a result of porous flow of a metasomatizing melt/fluid through the mantle (e.g. Navon and Stolper 1987; Bodinier et al., 1990, 2004; Godard et

al., 1995; Zanetti et al., 1996; Vernieres et al. 1997; Ionov et al., 2002). Elemental variations in the longest profile GV8 are consistent with such a chromatographic effect. Figure 8a displays the chondrite-normalized concentrations of La, Sm and Yb in clinopyroxene through the wall-rock and host peridotite of profile GV8. After an overall REE enrichment (*first step*, see above), concentrations of Yb and Sm decrease towards unmodified peridotite values whereas La is still at relatively invariably high concentrations (Fig. 8a). Figure 8b shows that Sm and Yb increase to a greater extent than La in *first step*, resulting in a decrease of La_N/Sm_N and La_N/Yb_N ratios. Once percolating melt volume is drastically reduced though crystallization, chromatographic fractionation is reflected by the progressive increase of La_N/Sm_N and La_N/Yb_N ratios with distance (Fig. 8b). Therefore, results of numerical modeling at very low melt/peridotite ratio (*second step*) simulate the chromatographic fractionation and successfully reproduce the documented trace element variations in clinopyroxene along the profile GV8 (Fig. 8a,b).

During chromatographic fractionation, less incompatible elements (e.g. Yb) are expected to reach equilibrium with the percolated peridotite matrix at shorter distances than the more incompatible ones (e.g. La). This, in turn, controls the width of the metasomatic fronts for different elements during melt-peridotite interaction (e.g. Bodinier et al., 1990; Zanetti et al., 1996). Outcrop dimensions prevented a further extension of this profile and the total width of REE modification in host peridotite via pyroxenite melt infiltration could not be determined. Nevertheless, it is remarkable that in the longest profile GV8 the metasomatic effects induced by pyroxenite emplacement involved up to 23 cm of the host peridotite, i.e. more than 3 times the thickness of the pyroxenite layer itself. Petrographic observations combined with results of the here presented numerical simulation provide strong constraints that reactive percolation of melt from pyroxenite acted as the leading mechanism in the modification of the trace element composition of the host peridotite.

7.3 Nature of mantle heterogeneities and implication for basalt production

Although melting of a mixed pyroxenite-peridotite source is now widely accepted for the genesis of Ocean Island Basalts (OIB; i.e. Sobolev et al., 2007; Mallik and Dasgupta, 2012), as well as for MORB (Sobolev et al., 2007; Lambart et al., 2012, 2016), major questions still remain to be answered. They mostly concern the nature and the length-scale of the enriched component and their efficiency in affecting basalt petrogenesis. Direct sampling of pyroxenites in the oceanic mantle is scarce and veined pyroxenite-peridotite mantle proxies are rarely documented. If low-T solidus components are involved in mantle melting and basalt production, they could be completely

consumed by melting, explaining the lack of pyroxenite relicts in the oceanic residual mantle. Indeed, very few pyroxenites have been sampled in abyssal peridotites and all have been ascribed to late-stage melt infiltration in a conductively cooling mantle (Constantin et al., 1995; Kempton and Stephens, 1997; Hebert et al., 2001; Chazot et al., 2005; Dantas et al., 2007, Warren et al., 2009; Laukert et al., 2014), hence they cannot provide direct information of the original pyroxenite-like heterogeneity in the source mantle before melting (Warren, 2016).

Nevertheless, the existence of isotopically-enriched domains in the mantle source has been often invoked to explain the "enriched" end of the isotopic MORB variation that is not reflected by the isotopic composition of abyssal peridotites, the latter representing the residues of melting that formed MORB (e.g., Salters & Dick, 2002; Liu et al., 2008; Paulick et al., 2010; Hoernle et al., 2011; Byerly & Lassiter, 2014; Mallick et al., 2015). This isotopic decoupling has been attributed in many cases to the involvement of "enriched" component(s) dispersed in the host peridotite mantle (e.g. Salters & Dick, 2002). Gale et al. (2013) by compiling a global MORB data set have chemically defined the Enriched (E)-MORBs ($La_N/Sm_N > 1.5$) and highlighted that many of them occur far from plume-influenced ridge segments. Such E-MORBs that are not obviously related to any mantle plume, are scattered and considered to reflect mantle sources including a small amount of pyroxenite (Niu et al., 1999, 2002; Waters et al., 2011) or modified by deep interaction with low-degree partial melts (Donnelly et al., 2004; Hemond et al., 2006; Nauret et al., 2006; Gale et al., 2014). However, the origin and physical form of these heterogeneities in the MORB mantle sources are today far from being discerned. A wide view held is that the enriched component may occur as small-scale dikes/veins in the ambient depleted peridotitic matrix (e.g. Niu et al., 2002; Paulick et al., 2010; Brunelli et al., 2018), but the knowledge of how, where and when these dikes/veins actually formed is scarce.

Our work provides direct observations of short-length-scale heterogeneities in the upper mantle, and constrains the processes by which the upper mantle can be chemically modified by interaction with pyroxenite-derived melts. Borghini et al. (2013) showed that over sufficient time, pyroxenite-driven chemical modification of the Ligurian peridotites led to enriched Nd-isotopic compositions, making these veined mantle domains a potential source of E-MORBs. The mantle sequence described here thus constitutes a proxy for a MORB-type "veined" mantle and potentially provides insights on the nature of heterogeneous sources of oceanic basalts. This agrees well with recent models of basalt petrogenesis at mid-ocean ridges, which assume that the MORB source is represented by a peridotitic mantle modified by melt-rock interaction and melt intrusion, leading to a pyroxenite-peridotite "hybrid" source, before it starts to melt and produce basalts (le Roux et al.,

2002; Donnelly et al., 2004; Sobolev et al., 2005; Lambart et al., 2012). A similar scenario has been proposed for the genesis of OIBs (Mallik & Dasgupta, 2012).

A critical aspect of the role of mantle heterogeneities in mantle melting concerns their efficiency in influencing the chemistry of oceanic basalts. Together with their enriched chemical/isotopic signature and the relatively high melt productivity (directly correlated to their bulk fertility, Lambart et al., 2016), the percentage of a pyroxenite component is thought to strongly control the chemistry of erupted melts. Liu & Liang (2017) have modelled melt generation and extraction from a heterogeneous source region of MORB. Their results indicate that pyroxenite-derived isotopic signatures can survive only if they derive from kilometer-scale domains because larger size and higher incompatible element abundance are more likely to survive mixing processes. Kilometer-scale heterogeneities have also been suggested by the distribution of Hf isotopic ratio anomalies in basalts along the southeast Indian Ridge (Graham et al., 2006), although the nature of these isotopically enriched domains is not clear. However, direct observations of large-scale primary pyroxenites or melting residues of such large domains in the oceanic mantle are rarely observed (e.g. Warren, 2016). In contrast, mantle sources consisting of small, tabular low-T solidus pyroxenites finely dispersed in peridotite, have been proposed to explain the contrasting degrees of partial melting degrees inferred from paired basalt - abyssal peridotite sections of the Vema fracture zone (26Ma long profile at ~11°N MAR) by Brunelli et al. (2018).

Kogiso et al. (2004) proposed that the style of melting and melt transport associated with pyroxenite sources depend on the size of the pyroxenite bodies and concluded that, assuming a considerable range of physical parameters, pyroxenite domains with submeter to a few meter width can produce melts with distinctive geochemical signatures under typical mantle melting conditions.

Because of the limited dimensions of the outcrops of pyroxenite-peridotite assemblages in the External Ligurides, chemical profiles could not be extended beyond 23 cm in this study so that the total length of trace element perturbation in the peridotite related to pyroxenite-derived melt percolation has not been constrained. Nevertheless, results of this work reveal that the emplacement of few-cm-sized pyroxenite veins by deep melt infiltration is able to metasomatize at least 23 cm of host peridotites. Considering that metasomatism extends into both sides of the host peridotite, REE-enriched aureoles of about half a meter form from relatively thin pyroxenite veins (e.g. GV8 is 5-6 cm wide). Here, we want to emphasize that centimeter-scale pyroxenite components in the mantle peridotite matrix can result in chemical/isotopic heterogeneity much larger than their own size.

Meter-scale portions of intensely veined mantle made of enriched wall-rock peridotite associated with rather refractory pyroxenites (relatively low alkali contents and high Mg-numbers) will produce melts with Fe/Mg very close to that of a peridotitic mantle (e.g. Lambart et al., 2013;

Borghini et al., 2017) but with an increasingly enriched Nd isotopic signature with increasing age of metasomatism (Borghini et al., 2013). Such melts are not highly reactive with lithospheric mantle peridotites and represent a good vehicle to bring up the geochemical and isotopic message from deeper heterogeneities, as required in the recent models of MORB petrogenesis (e.g. Lambart et al., 2012; Lambart, 2017).

We documented the first study case of a natural fertile mantle chemically modified by MORB-type pyroxenite emplacement. Our field-based work sheds light on the fundamental role of melt-peridotite reaction in generating a hybrid heterogeneous mantle source containing refertilized peridotite. The latter may have much larger volume than the associated pyroxenite and represents an enriched trace element and Nd-isotope component (more enriched than the pyroxenite component itself), capable to transmit a E-MORB signature. Therefore, this study offers a unique example of veined mantle source resulting from deep melt infiltration and melt-peridotite reaction invoked to explain E-MORB occurrence at ocean ridges and in models of MORB petrogenesis (e.g. Le Roux et al., 2002; Donnely et al., 2004; Waters et al., 2011; Lambart et al., 2012)

If heterogeneous mantle is rising beneath mid-ocean ridges, its low-T solidus components are subject to early selective melting and their resulting partial melts are expected to react with overlying mantle peridotite. This process is likely to occur several times, at different depths, during mantle ascent and prior to oceanic basalt generation and involves various types of heterogeneities (and thus melts with varying compositions) producing a large range of hybrid mantle rocks. Recycled pyroxenitic materials are therefore unlikely to be directly involved in the generation of oceanic basalts, rather a previously metasomatized/refertilized mantle is expected to reach the oceanic melting region (Lambart, 2017).

The interaction between pyroxenite-derived melt and ambient peridotite is the key process in modifying significant mantle portions that later will be sources of oceanic magmas. Results of this work provide a rare field-based example of such melt infiltration-induced mantle modification.

Acknowledgments

Andrea Risplendente is thanked for technical assistance during the work at electron microprobe. Constructive and helpful reviews by M. Perfit and one anonymous referee improved the manuscript and are gratefully acknowledged. We also thank the editorial handling by Catherine Chauvel. This work was financially supported by the Italian Ministry of Education, University and Research (MIUR) [PRIN-2015C5LN35] "Melt rock reaction and melt migration in the MORB mantle through combined natural and experimental studies.

References

Allègre, C.J., Turcotte, D.L., 1986. Implications of a two-component marble-cake mantle: Nature 323, 123–127.

Anders, E., Grevesse, N., 1989. Abundances of the elements: meteoric and solar. Geochim. Cosmochim. Acta 53, 197–214.

Bill, M., O'Dogherty, L., Guex, J., Baumgartner, P.O., Masson, H., 2001. Radiolarite ages in the Alpine-Mediterranean ophiolites: constraints on the oceanic spreading and the Tethys-Atlantic connection. Geological Society of American Bulletin 113, 129–143.

Bodinier, J.-L., Guiraud, M., Fabries, J., Dostal, J., Dupuy, C., 1987a. Petrogenesis of layered pyroxenites from the Lherz, Freychinede and Prades ultramafic bodies (Ariege, French Pyrenees). Geochim. Cosmochim. Acta 51, 279–290.

Bodinier, J.-L., Fabries, J., Lorand, J.-P., Dostal, J., Dupuy, C., 1987b. Geochemistry of amphibole pyroxenite veins from the Lherz and Freychinede ultramafic bodies (Ariege, French Pyrenees). Bull. Mineral. 110, 345–358.

Bodinier, J.-L., Vasseur, G., Vernieres, J., Dupuy, C., Fabries, J., 1990. Mechanisms of mantle metasomatism: geochemical evidence from the Lherz orogenic peridotite. J. Petrol. 31, 597–628.

Bodinier, J.L., Menzies, M.A., Shimizu, N., Frey, F.A., McPherson, E., 2004. Silicate, hydrous and carbonate metasomatism at Lherz, France: Contemporaneous derivatives of silicate melt-harzburgite reaction. J. Petrol. 45, 299–320.

Bodinier, J.-L., Garrido, C.J., Chanefo, I., Bruguier, O., Gervilla, F., 2008. Origin of pyroxenite-peridotite veined mantle by refertilization reactions: Evidence from the Ronda peridotite (Southern Spain). J. Petrol. 49, 999–1025.

Borghini, G., Fumagalli, P., Rampone, E., 2011. The geobarometric significance of plagioclase in mantle peridotites: A link between nature and experiments. Lithos 126, 42–53.

Borghini, G., Rampone, E., Zanetti, A., Class, C., Cipriani, A., Hofmann, A.W., Goldstein S., 2013. Meter-scale Nd isotopic heterogeneity in pyroxenite-bearing Ligurian peridotites encompasses global-scale upper mantle variability. Geology 41, 1055–1058.

Borghini, G., Rampone, E., Zanetti, A., Class, C., Cipriani, A., Hofmann, A.W., Goldstein S., 2016. Pyroxenite layersin the Northern Apennines upper mantle (Italy) – Generation by pyroxenite melting and melt infiltration. J. Petrol. 57, 625–653.

Borghini, G., Fumagalli, P., Rampone, E., 2017. Partial melting experiments on a natural pyroxenite at 1 and 1.5 GPa: insights on the role of secondary pyroxenites in basalts generation. Contrib. Mineral. Petrol. 172, 70.

Borghini, G., Fumagalli, P., Rampone, E., 2017. Interactions between peridotite and pyroxenite-derived melts at mantle conditions: an experimental study at 2 GPa. American Geophysical Union, Fall Meeting 2017, abstract #V33H-05.

Borghini, G., Fumagalli, P., 2018. Subsolidus phase relations in a mantle pyroxenite: an experimental study from 0.7 to 1.5 GPa. Eur. J. Mineral. 30, 333–348.

Byerly, B.L., Lassiter, J.C., 2014. Isotopically ultradepleted domains in the convecting upper mantle: implications for MORB petrogenesis. Geology 42, 203–206.

Brunelli, D., Seyler, M., Cipriani, A., Ottolini, L., Bonatti, E., 2006. Discontinuous melt extraction and weak refertilization of mantle peridotites at the Vema lithospheric section (Mid- Atlantic Ridge). J. Petrol. 47, 745–771.

Brunelli, D., Seyler, M., 2010. Asthenospheric percolation of alkaline melts beneath the St. Paul region (Central Atlantic Ocean). Earth Planet. Sci. Lett. 289, 393–405.

Brunelli, D., Paganelli, E., Seyler, M., 2014. Percolation of enriched melts during incremental open-system melting in the spinel eld: a REE approach to abyssal peridotites from the Southwest Indian Ridge. Geochim. Cosmochim. Acta 127, 190–203.

Brunelli, D., Cipriani, A., Bonatti, E., 2018. Thermal effects of pyroxenites on mantle melting below mid-ocean ridges. Nature Geoscience 11, 520–525.

Chazot, G., Charpentier, S., Kornprobst, J., Vannucci, R., Luais, B., 2005. Lithospheric mantle evolution during continental break-up: the West Iberia non-volcanic passive margin. J. Petrol. 46, 2527–2568.

Constantin, M., Hekinian, R., Ackermand, D., Stoffers, P., 1995. Mafic and ultramafic intrusions into upper mantle peridotites from fast spreading centers of the Eastern Microplate (South East Pacific). In: Vissers, R.L.M., Nicolas, A. (Eds.), Mantle and lower crust exposed in oceanic ridges and in ophiolites. Kluwer, Dordrecht, pp. 71–120.

Dantas, C., Ceuleneer, G., Gregoire, M., Python, M., Freydier, R., Warren, J., Dick, H.J.B., 2007. Pyroxenites from the Southwest Indian Ridge, 9–16°E: cumulates from incremental melt fraction produced at the top of a cold melting regime. J. Petrol. 48, 647–660.

Donnelly, K. E., Goldstein, S. L., Langmuir, C. H., Spiegelman, M., 2004. Origin of enriched ocean ridge basalts and implications for mantle dynamics. Earth Planet. Sci. Lett. 226, 347–366.

Fabries, J., Lorand, J.-P., Guiraud, M., 2001. Petrogenesis of the amphibole-rich veins from Lherz orogenic lherzolite massif (Easter Pyrenees, France): a case study for the origin of orthopyroxene-bearing amphibole pyroxenites in the lithospheric mantle. Contrib. Mineral. Petrol. 140, 383–403.

Gale, A., Dalton, C.A., Langmuir, C.H., Su, Y., Schilling, J.G., 2013. The mean composition of ocean ridge basalts. Geochem. Geophys. Geosyst. 14, 489–518.

Gale, A., Langmuir, C.H., Dalton, C.A., 2014. The global systematics of ocean ridge basalts and their origin. J. Petrol. 55, 1051–1082.

Garrido, C.J., Bodinier, J.L., 1999. Diversity of mafic rocks in the Ronda peridotite: evidence for pervasive melt–rock reaction during heating of subcontinental lithosphere by upwelling asthenosphere. J. Petrol. 40, 729–754.

Gysi, A.P., Jagoutz, O., Schmidt, M.W., Targuisti, K., 2011. Petrogenesis of pyroxenites and melt infiltrations in the ultramafic complex of Beni Boussera, Northern Morocco. J. Petrol. 52, 1676–1735.

Godard, M., Bodinier, J.L., Vasseur, G., 1995. Effects of mineralogical reactions on trace element redistributions in mantle rocks during percolation processes: a chromatographic approach. Earth Planet. Sci. Lett. 133, 449–461.

Godard, M., Jousselin, D., Bodinier, J.-L., 2000. Relationships between geochemistry and structure beneath a palaeo-spreading centre: A study of the mantle section in the Oman Ophiolite. Earth Planet. Sci. Lett. 180, 133–148.

Godard, M., Lagabrielle, Y., Alard, O., Harvey, J., 2008. Geochemistry of the highly depleted peridotites drilled at ODP Sites 1272 and 1274 (Fifteen-Twenty Fracture Zone, Mid-Atlantic Ridge): implications for mantle dynamics beneath a slow spreading ridge. Earth Planet. Sci. Lett. 267, 410–425.

Graham, D.W., Blichert-Toft, J., Russo, C.J., Rubin, K.H., Albarede, F., 2006. Cryptic striations in the upper mantle revealed by hafnium isotopes in southeast Indian ridge basalts. Nature 440, 199–202.

Gysi, A.P., Jagoutz, O., Schmidt, M.W., Targuisti, K., 2011. Petrogenesis of pyroxenites and melt infiltrations in the ultramafic complex of Beni Boussera, Northern Morocco. J. Petrol. 52, 1676–1735.

Hémond, C., Hofmann, A.W., Vlastelic, I., Nauret, F., 2006. Origin of MORB enrichment and relative trace element compatibilities along the Mid-Atlantic Ridge between 10° and 24°N. Geochem. Geophys. Geosyst. 7, Q12010.

Hébert, R., Gueddari, K., LaFlèche, M.R., Beslier, M.O., Gardien, V., 2001. Petrology and geochemistry of exhumed peridotites and gabbros at non-volcanic margins: ODP Leg 173 West Iberia ocean–continent transition zone. Geological Society London, Special Publications 187, 161–189.

Herzberg, C., 2011. Identification of source lithology in the Hawaiian and Canary Islands: implications for origins. J. Petrol. 52, 113–146.

Hidas, K., Garrido, C., Tommasi, A., Padron-Navarta, J.A., Thielmann, M., Konc, Z., Frets, E., Marchesi, C., 2013. Strain localization in pyroxenite by reaction-enhanced softening in the shallow subcontinental lithospheric mantle. J. Petrol. 54, 1997–2031.

Hirschmann, M.M., Stolper, E.M., 1996. A possible role for garnet pyroxenite in the origin of the 'garnet signature' in MORB. Contrib. Mineral. Petrol. 124, 185–208.

Hoernle, K., Hauff, F., Kokfelt, T.F., Haase, K., Garbe-Shonberg, D., Werner, R., 2011. On- and off-axis chemical heterogeneities along the South Atlantic Mid-Ocean-Ridge (5–11°S): shallow or deep recycling of ocean crust and/or intraplate volcanism? Earth Planet. Sci. Lett. 306, 86–97.

Ionov, D.A., Savoyant, L., Dupuy, C., 1992. Application of the ICP-MS technique to trace element analysis of peridotites and their minerals. Geostand. Newsl. 16, 311–315.

Ionov, D.A., Bodinier, J.L., Mukasa, S.B., Zanetti, A., 2002. Mechanisms and sources of mantle metasomatism: major and trace element conditions of peridotite xenoliths from Spitzbergen in the context of numerical modelling. J. Petrol. 43, 2219–2259.

Ionov, D.A., Chanefo, I., Bodinier, J.L., 2005. Origin of Fe-rich lherzolites and wehrlites from Tok, SE Siberia by reactive melt per- colation in refractory mantle peridotites. Contrib. Mineral. Petrol. 150, 335–353.

Ishimaru, S., Arai, S., Tamura, A., 2017. Clinopyroxenite dykes within a banded unit in the basal section of the northern part of the Oman ophiolite: a record of the latest deep-seated magmatism. Lithos 292-293, 334–347.

Jochum, K.P., Seufert, H.M., Thirwall, M.F., 1990. High-sensitivity Nb analysis by spark-source mass spectrometry (SSMS) and calibration of XRF Nb and Zr. Chem. Geol. 81, 1–16.

Kaczmarek, M.A., Bodinier, J.L., Bosch, D., Tommasi, A., Dautria, J.M., Kechid, S.A., 2016. Metasomatized mantle xenoliths as a record of the lithospheric mantle evolution of the northern edge of the ahaggar swell, in teria (Algeria). J. Petrol. 57, 345–382.

Kelemen, P.B., Whitehead, J.A., Aharonov, E., Jordahl, K.A., 1995. Experiments on flow focusing in soluble porous-media, with applications to melt extraction from the mantle. J. Geophys. Res. 100, 475–496.

Kempton, P.D., Stephens, C.J., 1997. Petrology and geochemistry of nodular websterites inclusions in harzburgite, Hole 920D, in Karson, J.A., et al., eds., Proceedings of the Ocean Drilling Program, Scientific results 153: College Station, Texas, Ocean Drilling Program, p. 321–331.

Keshav, S., Sen, G., Presnall, D.C., 2007. Garnet-bearing xenoliths from Salt Lake Crater, Oahu, Hawaii: high-pressure fractional crystallisation in the oceanic mantle. J Petrol. 48, 1681-1724.

Kogiso, T., Hirschmann, M.M., Pertermann, M., 2004a. High-pressure partial melting of mafic lithologies in the mantle. J. Petrol. 45, 2407–2422.

Kogiso, T., Hirschmann, M.M., Reiners, W., 2004b. Length scales of mantle heterogeneities and their relationship to ocean island basalt geochemistry. Geochim. Cosmochim. Acta 68, 345–360.

Kogiso, T., Hirschmann, M.M., 2006. Partial melting experiments of bimineralic eclogite and the role of recycled mafic oceanic crust in the genesis of ocean island basalts. Earth Planet. Sci. Lett. 249, 188–199.

Kornprobst, J., Piboule, M., Roden, M., Tabit, A., 1990. Corundum-bearing garnet clinopyroxenites at Beni Bousera (Morocco): original plagioclase-rich gabbros recrystallized at depth within the mantle? J. Petrol. 31, 717–745.

Lambart, S., Laporte, D., Provost, A., Schiano, P., 2012. Fate of pyroxenite-derived melts in the peridotitic mantle: thermodynamic and experimental constraints. J. Petrol. 53, 451–476.

Lambart, S., Laporte, D., Schiano, P., 2013. Markers of the pyroxenite contribution in the major-element compositions of oceanic basalts: Review of the experimental constraints. Lithos 160-161, 14–36.

Lambart, S., Baker, M.B., Stolper, E.M., 2016. The role of pyroxenite in basalt genesis: Melt-PX, a melting parameterization for mantle pyroxenites between 0.9 and 5 GPa. J. Geophys. Res. 121, 5708–5735.

Lambart, S., 2017. No direct contribution of recycled crust in Icelandic basalts. Geochemical Perspectives Letters 4, 7–12.

Laukert, G., Von Der Handt, A., Hellebrabd, E., Snow, J.E., Hoppe, P., Klugel, A., 2014. High-pressure reactive melt stagnation recorded in abyssal pyroxenites from the ultraslow-spreading Lena Trough, Artic Ocean. J. Petrol. 55, 427–458.

Lemoine, M., Tricart, P., Boillot, G., 1987. Ultramafic and gabbroic ocean floor of the Ligurian Tethys (Alps, Corsica and Apennines): in search of a genetic model. Geology 15, 622–625.

le Roex, A., Class, C., 2014. Metasomatism of the Pan-African lithospheric mantle beneath the Damara Belt, Namibia, by the Tristan mantle plume: geochemical evidence from mantle xenoliths. Contrib. Mineral. Petrol. 168, 1046.

Le Roux, P.J., le Roex, A.P., Schilling, J.G., Shimizu, N., Perkins, W.W., Pearce, N.J.G., 2002. Mantle heterogeneity beneath the southern Mid-Atlantic Ridge: trace element evidence for contamination of ambient asthenospheric mantle. Earth Planet. Sci. Lett. 203, 479–498.

Le Roux, V., Bodinier, J.-L., Alard, O., O'Reilly, S.Y., Griffin, W.L., 2009. Isotopic decoupling during porous melt flow: a case-study in the Lherz peridotite. Earth Planet. Sci. Lett. 279, 76–85.

Liu, C., Snow, J. E., Hellebrand, E., Brugmann, G., Von Der Handt, A., Buchl, A., Hofmann, A.W., 2008. Ancient, highly heterogeneous mantle beneath Gakkel Ridge, Arctic Ocean. Nature 452, 311–316.

Liu, B., Liang, Y., 2017. E prevalence of kilometer-scale heterogeneity in the source region of MORB upper mantle. Sci. Adv. 3, e1701872.

Mallik, A., Dasgupta, R., 2012. Reaction between MORB-eclogite derived melts and fertile peridotite and generation of ocean island basalts. Earth Planet. Sci. Lett. 329-330, 97–108.

Mallik, S., Standish, J.J., Bizimis, M., 2015. Constraints on the mantle mineralogy of an ultra-slow ridge: hafnium isotopes in abyssal peridotites and basalts from the 9-25°E Southwest Indian Ridge. Earth Planet. Sci. Lett. 410, 43–53.

Marchesi, C., Garrido, C.J., Bosch, D., Bodinier, J.L., Gervilla, F., Hidas, K., 2013. Mantle refertilization by melts of crustal-derived garnet pyroxenite: Evidence from the Ronda peridotite massif, southern Spain. Earth Planet. Sci. Lett. 362, 66–75.

Marchesi, C., Konc, Z., Garrido, C.J., Bosch, D., Hidas, K., Varas-Reus, M.I., Acosta-Vigil, A., 2017. Multi-stage evolution of the lithospheric mantle beneath the westernmost Mediterranean: geochemical constraints from peridotite xenoliths in the eastern Betic Cordillera (SE Spain). Lithos 276, 75–89.

Marroni, M., Meneghini, F., Pandolfi, L., 2010. Anatomy of the Ligure-Piemontese subduction system: evidence from Late Cretaceous-middle Eocene convergent margin deposits in the Northern Apennines, Italy. International Geology Review 52, 1160–1192.

Mazzucchelli, M., Zanetti, A., Rivalenti, G., Vannucci, R., Correia, C.T., Tassinari, C.C.G., 2010. Age and geochemistry of mantle peridotites and diorite dykes from the Baldissero body: Insights into the Paleozoic-Mesozoic evolution of the Southern Alps. Lithos 119, 485–500.

McPherson, E., Thirlwall, M.F., Parkinson, I.J., Menzies, M.A., Bodinier, J.L., Woodland, A., Bussod, G., 1996. Geochemistry of metasomatism adjacent to amphibole-bearing veins in the Lherz peridotite massif. Chem. Geol. 131, 135–157.

Menzies, M.A., Rogers,N., Tindle, A., Hawkesworth, C.J., 1987. Metasomatic and enrichment processes in lithospheric peridotites, an effect of asthenosphere-lithosphere interaction. Mantle Metasomatism, 313–361.

Montanini, A., Tribuzio, R., Anczkiewicz, R., 2006. Exhumation history of a garnet pyroxenite-bearing mantle section from a continent-ocean transition (Northern Apennine ophiolites, Italy). J. Petrol. 47, 1943–1971.

Montanini, A., Tribuzio, R., Thirlwall, M., 2012. Garnet clinopyroxenite layers from the mantle sequences of the Northern Apennine ophiolites (Italy): Evidence for recycling of crustal material. Earth Planet. Sci. Lett. 351–352, 171–181.

Montanini, A., Tribuzio, R., 2015. Evolution of recycled crust within the mantle: constraints from the garnet pyroxenites of the External Ligurian ophiolites (northern Apennines, Italy). Geology 43, 911–914.

Morishita, T., Arai, S., 2001. Petrogenesis of corundum-bearing mafic rock in the Horoman Peridotite Complex, Japan. J. Petrol. 42, 1279–1299.

Morishita, T., Arai, S., Gervilla, F., Green, D.H., 2003. Closed-system geochemical recycling of crustal materials in the upper mantle. Geochim. Cosmochim. Acta 67, 303–310.

Mukasa, S.B., Shervais, J.W., 1999. Growth of sub-continental lithosphere: Evidence from repeated injections in the Balmuccia lherzolite massif, Italian Alps. Lithos 48, 287–316.

Mundl, A., Ntaflos, T., Ackerman, L., Bizimis, M., Bjerg, E.A., Wegner, W., Hauzenberger, C.A., 2016. Geochemical and Os-Hf-Nd-Sr isotopic characterization of North Patagonian Mantle xenoliths: implications for extensive melt extraction and percolation processes. J. Petrol. 57, 685–715.

Müntener, O., Piccardo, G.B., 2003. Melt migration in ophiolites: the message from Alpine–Apennine peridotites and implica- tions for embryonic ocean basins. In: Dilek, Y., Robinson, P.T. (Eds.), Ophiolites in Earth HistoryGeol. Soc. London Spec. Publ., vol. 218, pp. 69–89.

Müntener, O., Pettke, T., Desmurs, L., Meier, M., Schaltegger. U., 2004. Refertilization of mantle peridotite in embryonic ocean basins: trace element and Nd-isotopic evidence and implications for crust-mantle relationships. Earth Planet. Sci. Lett. 221, 293–308.

Nauret, F., Abouchami, W., Galer, S.J.G., Hofmann, A.W., Hemond, C., Chauvel, C., Dyment, J., 2006. Correlated trace element-Pb isotope enrichments in Indian MORB along 18-20°S, Central Indian Ridge. Earth Planet. Sci. Lett. 245, 137–152.

Navon, O., Stolper, E., 1987. Geochemical consequence of melt percolation: the upper mantle as a chromatographic column. J. Geol. 95, 285–307.

Niu, Y., Collerson, K.D., Batiza, R., Wendt, J.I., Regelous, M., 1999. The origin of E-Type MORB at ridges far from mantle plumes: The East Pacific Rise at 11820'N. J. Geophys. Res. 104, 7067–7087.

Niu, Y., Regelous, M., Wendt, J.I., Batiza, R., O'Hara, M.J., 2002. Geochemistry of near-EPR seamounts: Importance of source vs process and the origin of enriched mantle component. Earth Planet. Sci. Lett. 199, 329–348.

Niu, Y., 2004. Bulk-rock major and trace element compositions of abyssal peridotites: Implications for mantle melting, melt extraction and post-melting processes beneath ocean ridges. J. Petrol. 45, 2423–2458.

Paulick, H., Mueker, C., Schluth, S., 2010. The influence of small-scale mantle heterogeneities on Mid-Ocean Ridge volcanism: Evidence from the southern Mid-Atlantic Ridge (7 degrees 30'S to 11 degrees 30'S) and Ascension Island. Earth Planet. Sci. Lett. 296, 299–310.

Pearson, D.G., Davies, G.R., Nixon, P.H., 1993. Geochemical constraints on the petrogenesis of diamond facies pyroxenites from the Beni Bousera peridotite massif, North Morocco. J. Petrol. 34, 125–172.

Pearson, D.G., Nowell, G.M., 2004. Re-Os and Lu-Hf isotope constraints on the origin and age of pyroxenites from the Beni Bousera peridotite massif: implications for mixed peridotite-pyroxenite mantle source. J. Petrol. 45, 439–455.

Piccardo, G.B., Müntener, O., Zanetti, A., Pettke, T., 2004. Ophiolitic peridotites of the Alpine–Appenine system: mantle processes and geodynamic relevance. Int. Geol. Rev. 46, 1119–1159.

Piccardo, G.B., Zanetti, A., Poggi, E., Spagnolo, G., Müntener, O., 2007. Melt/peridotite interaction in the Lanzo South peridotite: field, textural and geochemical evidence. Lithos 94, 181–209.

Pinter, Z., Rosenthal, A., Frost, D.J., Mccammon, C.A., Höfer, H.E., Yaxley, G.M., Berry, A., Woodland, A.B., Vasilyev, P., Pearson, G.D., 2015. High pressure experimental investigation of the interaction between partial melts of eclogite and mantle peridotite during upwelling. American Geophysical Union, Fall Meeting 2015, abstract #V33C-3113.

Rampone E., Bottazzi P., Ottolini L., 1991. Complementary Ti and Zr anomalies in orthopyroxene and clinopyroxene from mantle peridotites. Nature 354, 518–521.

Rampone, E., Piccardo, G.B., Vannucci, R., Bottazzi, P., Ottolini, L., 1993. Subsolidus reactions monitored by trace element partitioning: the spinel- to plagioclasi-facies transition in mantle peridotites. Contrib. Mineral. Petrol. 115, 1–17.

Rampone, E., Hofmann, A.W., Piccardo, G.B., Vannucci, R., Bottazzi, P., Ottolini, L., 1995. Petrology, mineral and isotope geochemistry of the External Liguride peridotites (Northern Apennines, Italy). J. Petrol. 123, 61–76.

Rampone, E., Piccardo, G.B., Vannucci, R., Bottazzi, P., 1997. Chemistry and origin of ted melts in ophiolitic peridotites. Geochim. Cosmochim. Acta 61, 4557–4569.

Rampone, E., Piccardo, G.B., 2000. The ophiolite–oceanic lithosphere analogue: new insights from the Northern Apennines (Italy). In: Dilek, Y., Moores, E.M., Elthon, D., Nicolas, A. (Eds.), Ophiolites and Oceanic Crust: New Insights from Field Studies and the Oceanic Drilling Program. Geological Society of America Special Papers, 349, pp. 21–34.

Rampone, E., Romairone, A., Hofmann, A.W., 2004. Contrasting bulk and mineral chemistry in depleted peridotites: evidence for reactive porous flow. Earth Planet. Sci. Lett. 218, 491–506.

Rampone, E., Romairone, A., Abouchami, W., Piccardo, G.B., Hofmann, A.W., 2005. Chronology, petrology and isotope geochemistry of the Erro-Tobbio peridotites (Ligurian Alps, Italy): records of Late Palaeozoic lithospheric extension. J. Petrol. 46 (4), 799–827.

Rampone, E., Piccardo, G.B., Hofmann, A.W., 2008. Multi-stage melt-rock interaction in the Mt. Maggiore (Corsica, France) ophiolitic peridotites: microstructural and geochemical records. Contrib. Mineral. Petrol. 156, 453–475.

Rampone, E., Borghini, G., 2008. Melt migration and intrusion in the Erro-Tobbio peridotites (Ligurian Alps, Italy): insights on magmatic processes in extending lithospheric mantle. Eur. J. Mineral. 20, 573–585.

Rampone, E., Borghini, G., Basch, V., 2018. Melt migration and melt-rock reaction in the Alpine-Apennine peridotites: insights on mantle dynamics in extending lithosphere. Geoscience Frontiers, https://doi.org/10.1016/j.gsf.2018.11.001.

Rapp, R.P., Shimizu, N., Norman, M.D., Applegate, G.S., 1999. Reaction between slab-derived melts and peridotite in the mantle wedge: experimental constraints at 3.8 GPa. Chem. Geol. 160, 335–356.

Rapp, R.P., Norman, M.D., Laporte, D., Yaxley, G.M., Martin, H., Foley, S.F., 2010. Melt-rock reaction experiments at 3-4 GPa and petrogenesis of archean Mg-diorites (Sanukitoids). J. Petrol. 51, 1237–1266.

Rivalenti, G., Mazzucchelli, M., Vannucci, R., Hofmann, A.W., Ottolini, L., Obermiller, W., 1995. The relationship between websterite and peridotite in the Balmuccia peridotite massif (NW Italy) as revealed by trace element variations in clinopyroxene. Contrib. Mineral. Petrol. 121, 275–288.

Rosenthal, A., Yaxley, G.M., Green, D.H., Hermann, J., Kovacs, I., Spandler, C., 2014. Continuous eclogite melting and variable refertilization in upwelling heterogeneous mantle. Scientific Reports 4, 6099.

Salters, V.J.M., Dick, H.J.B., 2002. Mineralogy of the mid-ocean-ridge basalt source from neodymium isotopic composition of abyssal peridotites. Nature 418, 68–72.

Shervais, J.W., Mukasa, S.B., 1991. The Balmuccia orogenic lherzolite massif, Italy. J. Petrol. Spec. Vol., pp. 155–174.

Shorttle, O., Maclennan, J., 2011. Compositional trends of Icelandic basalts: implications for short-length scale lithological heterogeneity in mantle plumes. Geochem. Geophys. Geosyst. 12, Q11008.

Shorttle, O., Maclennan, J., Lambart, S., 2014. Quantifying lithological variability in the mantle. Earth Planet. Sci. Lett. 395, 24–40.

Sobolev, A.V., Hofmann, A.W., Sobolev, S.V., Nikogosian, I.K., 2005. An olivine-free mantle source of Hawaiian shield basalts. Nature 434, 590–597.

Sobolev, A.V., Hofmann, A.W., Kuzmin, D.V., Yaxley, G.M., Arndt, N.T., Chung, S.L., Danyushevsky, L.V., Elliott, T., Frey, F.A., Garcia, M.O., Gurenko, A.A., Kamenetsky, V.S., Kerr, A.C., Krivolutskaya, N.A., Matvienkov, V.V., Nikogosian, I.K., Rocholl, A., Sigurdsson, I.A., Sushchevskaya, N.M., Teklay, M., 2007. The amount of recycled crust in sources of mantle-derived melts. Science 316, 412–417.

Stracke, A., Salters, V.J.M., Sims, K.W.W., 1999. Assessing the presence of garnet–pyroxenite in the mantle sources of basalts through combined hafnium–neodymium–thorium isotope systematics. Geochem. Geophys. Geosyst. 1.

Takazawa, E., Frey, F.A., Shimizu, N., Saal, N., Obata, M., 1999. Polybaric petrogenesis of mafic layers in the Horoman peridotite complex, Japan. J. Petrol. 40, 1827–1831.

Tilhac, R., Ceuleneer, G., Griffin, W.L., O'Reilly, S.Y., Pearson, N.J., Benoit, M., Henry, H., Girardeau, J., Gregoire, M., 2016. Primitive arc magmatism and delamination: petrology and geochemistry og pyroxenites from the Cabo Ortegal Complex, Spain. J. Petrol. 57, 1921–1954.

Tilhac, R., Gregoire, M., W.L., O'Reilly, Griffin, S.Y., Henry, H., Ceuleneer, G., 2017. Sources and timing of pyroxenite formation in the sub-arc mantle: case study of the Cabo Ortegal Complex, Spain. Earth Planet. Sci. Lett. 474, 490–4502.

Van Acken, D., Becker, H., Walker, R.J., McDonough, W.F., Wombacher, F., Ash, R.D., Piccoli, P.M., 2010. Formation of pyroxenite layers in the Totalp ultramafic massif (Swiss Alps) – Insights from highly siderophile elements and Os isotopes. Geochim. Cosmochim. Acta 74, 661–683.

Varas-Reus, M.I., Garrido, C.J., Marchesi, C., Bosch, D., Hidas, K., 2018. Genesis of ultra-high pressure garnet pyroxenites in orogenic peridotites and its bearing on the compositional heterogeneity of the Earth's mantle. Geochim. Cosmochim. Acta 232, 303–328.

Varfalvy, V., Herbert, R., Bedard, J.H., 1996. Interactions between melt and upper-mantle peridotites in the North Arm Mountain Massif, Bay of Islands Ophiolite, Newfoundland,

Canada: implications for the genesis of boninites and related magmas. Chem. Geol. 129, 71–90.

Vernieres, J., Godard, M., Bodinier, J.L., 1997. A plate model for the simulation of trace element fractionation during partial melting and magma transport in the Earth's upper mantle. J. Geophys. Res. 102, 24771–24784.

Wang, C., Ji, Z., Gao, S., Zhang, J., Zheng S., 2010. Eclogite-melt/peridotite reaction: experimental constraints on the destruction mechanism of the North China Craton. Sci. China Earth Sci. 53, 797–809.

Wang, C., Liang, Y., Xu, W., Dygert, N., 2013. Effect of melt composition on basalt and peridotite interaction: laboratory dissolution experiments with applications to mineral compositional variations in mantle xenoliths from the North China Craton. Contrib. Mineral. Petrol. 166, 1469–l488.

Wang, C.G., Liang, Y., Dygert, N., Xu, W.L., 2016. Formation of orthopyroxenite by reaction between peridotite and hydrous basaltic melt: an experimental study. Contrib. Mineral. Petrol. 171, 77.

Warren, J.M., Shimizu, N., Sakaguchi, C., Dick, H.J.B., Nakamura, E., 2009. An assessment of upper mantle heterogeneity based on abyssal peridotite isotopic compositions. J. Geophys. Res. 114, B12203.

Warren, J.M., 2016. Global variations in abyssal peridotite compositions. Lithos 248–251, 193–219.

Waters, C.L., Sims, K.W.W., Perfit, M.R., Blichert-Toft, J., Blusztajn, J., 2011. Perspective on the genesis of E-MORB from chemical and isotopic heterogeneity at 9–10°N East Pacific Rise. J. Petrol. 52, 565–602.

Woodland, A.B., Kornprobst J., McPherson, E., Bodinier, J.L., Menzies, M.A., 1996. Metasomatic interactions in the lithospheric mantle: petrologic evidence from the Lherz massif, French Pyrenees. Chem. Geol. 134, 83–112.

Yaxley, G.M., Green, D.H., 1998. Reactions between eclogite and peridotite: mantle refertilisation by subduction of oceanic crust. Schweiz. Mineral. Petrogr. Mitt. 78, 243–255.

Yaxley, G.M., 2000. Experimental study of the phase and melting relations of homogeneous basalt + peridotite mixtures and implications for the petrogenesis of flood basalts. Contrib. Mineral. Petrol. 139, 326–338.

Yu, S., Xu, Y., Ma, J., Zheng, Y., Kuang, Y., Hong, L., Ge, W. & Tong, L. (2010). Remnants of oceanic lower crust in the subcontinental lithospheric mantle: trace element and Sr–Nd–O isotope evidence from aluminous garnet pyroxenite xenoliths from Jiaohe, Northeast China.

Earth Planet. Sci. Lett. 297, 413–422.

Yu, Y., Xu, W.L., Wang, C.G., 2014. Experimental studies of melt-peridotite reactions at 1–2 GPa and 1250–1400°C and their implications for trans- forming the nature of lithospheric mantle and for high-Mg signatures in adakitic rocks. Science China: Earth Sciences, 57, 415–427.

Zanetti, A., Vannucci, R., Bottazzi, P., Oberti, R., Ottolini, L., 1996. Infiltration metasomatism at Lherz as monitored by systematic ion- microprobe investigations close to a hornblendite vein. Chem. Geol. 134, 113–133.

FIGURE CAPTIONS

Figure 1. Field relations in Suvero and M.te Castellaro ultramafic bodies (External Liguride Units, Northertn Apennines, Italy). (a) Country-rock (pyroxenite-free) peridotite showing a well-developed mantle tectonite foliation. (b) Centimetres-thick pyroxenite layers embedded in mantle peridotite. (c) A representative spatially-controlled pyroxenite-peridotite profile in which the white lines indicate the size of wall-rock and host peridotite. Wall-rock peridotite is differentiated from host peridotite by the occurrence of large orthopyroxene blebs (see text for details). In the close-up view, a representative hand sample shows a thin orthopyroxene-rich rim at the pyroxenite-peridotite contact.

Figure 2. Photomicrographs of representative microstructures of External Liguride (EL) pyroxenite-peridotite sequences. (a) Brown spinel porphyroclast partially replaced by plagioclase and olivine from a country-rock peridotite. (b) Coarse green spinel surrounded by plagioclase-bearing neoblastic associations. (c) Orthopyroxene-rich boundary at the contact between pyroxenite layer and wall-rock peridotite. (d) Elongated relict of "hunter" green spinel intensely replaced by neoblastic associations made by plagioclase + olivine + amphibole, in wall-rock peridotite. (e) Large bleb of orthopyroxene in wall-rock peridotite.

Figure 3. Variation diagrams for SiO_2, Al_2O_3 and CaO (wt %) versus X_{Mg} [molar $Mg/(Mg + Fe^{2+}_{tot})$] for pyroxenites and peridotite from EL mantle sequences.

Figure 4. Chondrite-normalized rare earth element (REE plus Zr, Hf and Y) patterns for whole-rock peridotites from selected EL profiles and a representative country-rock peridotite. Normalizing values are from Anders and Grevesse (1989).

Figure 5. Variation of X_{Mg} versus Al (a) and Cr (b) (a.p.f.u.) in clinopyroxenes and X_{Cr} [molar Cr/(Cr + Al)] in spinels (c) from selected pyroxenite-peridotite profiles and country-rock

peridotites. Data have been collected from the cores of the largest clinopyroxene and spinel porphyroclasts.

Figure 6. Chondrite-normalized REE, Zr, Hf, Ti and Y patterns of clinopyroxene porphyroclasts from pyroxenite-peridotite profiles (BG14: a, BG22: b, GV8: c and d). The fields of clinopyroxene porphyroclasts from pyroxenites (orange field) and country-rock peridotites (light grey field) are reported for comparison. The orange field in (d) refers to the clinopyroxene composition along the entire profile GV8. Bar at right side of the REE patterns indicates the distance of the in-situ laser analyses from the pyroxenite–wall-rock peridotite contact. Normalizing values are from Anders and Grevesse (1989).

Figure 7. Results of numerical simulation of reactive porous flow (Plate Model of Vernieres et al., 1997). (a) Chondrite-normalized REE patterns of clinopyroxene porphyroclasts in wall-rock peridotite from profiles BG14 and GV8 and relative equilibrium liquids (dashed lines) computed by applying partition coefficients from Ionov et al. (2002). The calculated equilibrium liquids are used as initial reacting melts in the model. (b) Evolution of chondrite-normalized REE abundances in clinopyroxene resulting from Plate Model simulation of REE chemical gradient (*step 1*) observed in wall-rock peridotite BG14 (b) and wall-rock and host peridotites of profile GV8 (up to about 15 cm from the pyroxenite-peridotite contact) (c). (d) Evolution of chondrite-normalized REE abundances in clinopyroxene resulting from *step 2* of the Plate Model simulating the chemical gradient observed in GV8 host peridotite (from about 15 to 23 cm). Here we assume REE concentrations of liquid in the last *cell* of step 1 (*cell 10* in c) as starting reactive melt (from about 15 to 23 cm). Small colored numbers refer to the progressive *cells* of the model. See the text for details of input parameters and further explanation. Yellow field in (a) and (d) is defined by the chondrite-normalized REE patterns of clinopyroxene porphyroclasts in country-rock peridotites. Grey fields in (b), (c) and (d) are the REE chemical gradients measured in the selected profiles (BG14 and GV8). Yellow and grey fields refer to REE compositions of clinopyroxene from pyroxenite (associated to each profile) and country-rock peridotite, respectively. Normalizing values are from Anders and Grevesse (1989).

Figure 8. La_N, Sm_N and Yb_N concentrations (a) La_N/Sm_N and La_N/Yb_N ratios (b) (normalized to chondrite of Anders and Grevesse 1989) along the longest profile GV8 (0-23 cm). Measured data (filled symbols) are here compared to the results of numerical simulations described in Fig. 7 (dotted lines). Some input parameters used in the modeling are also reported; assimilated mass, crystallized mass; Φ_i is the initial porosity of the peridotite matrix. Symbols on the right side of diagram (a) refer to values from country-rock peridotite.

Figure1
Click here to download high resolution image

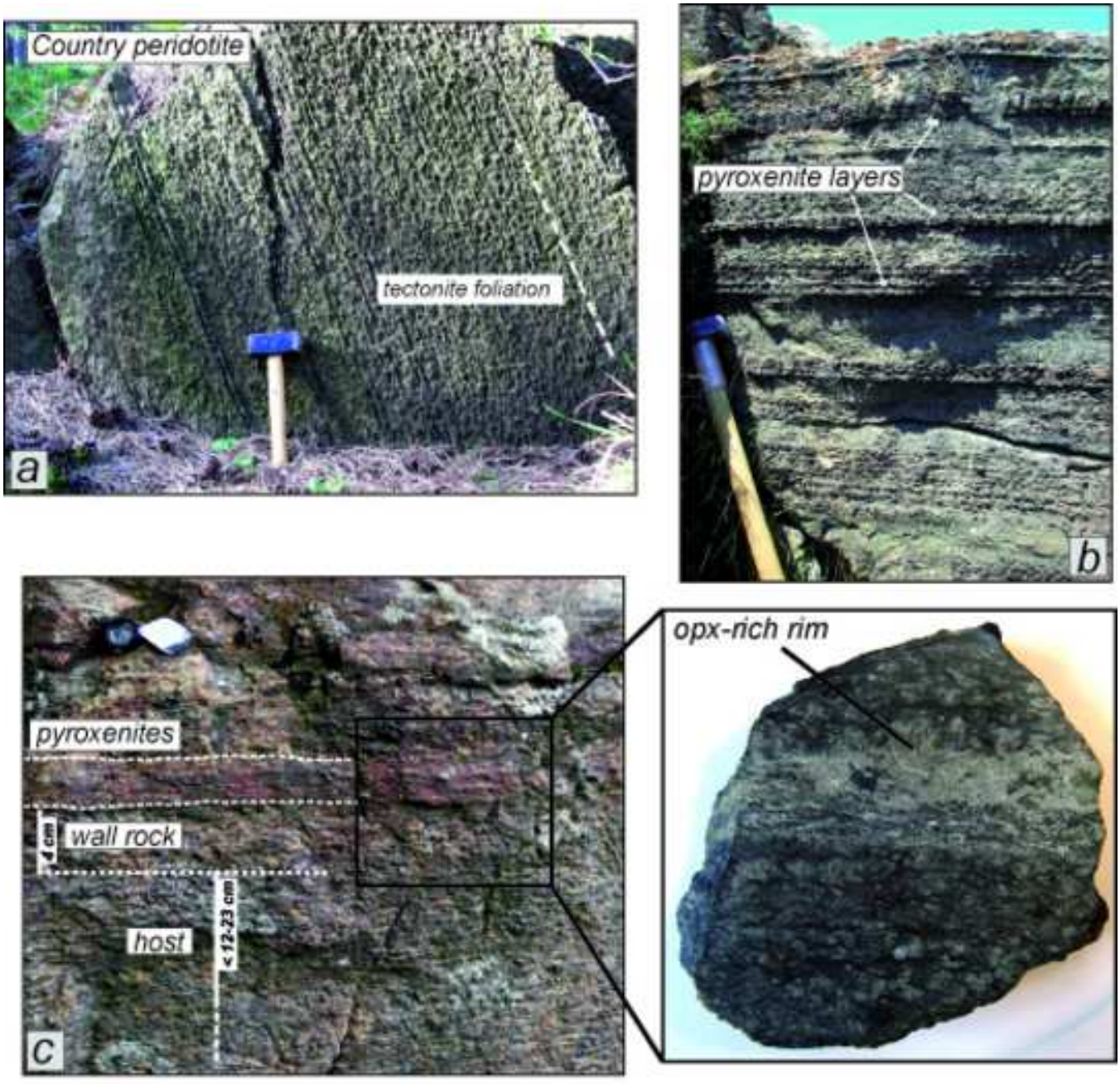

Figure 1

Figure2
Click here to download high resolution image

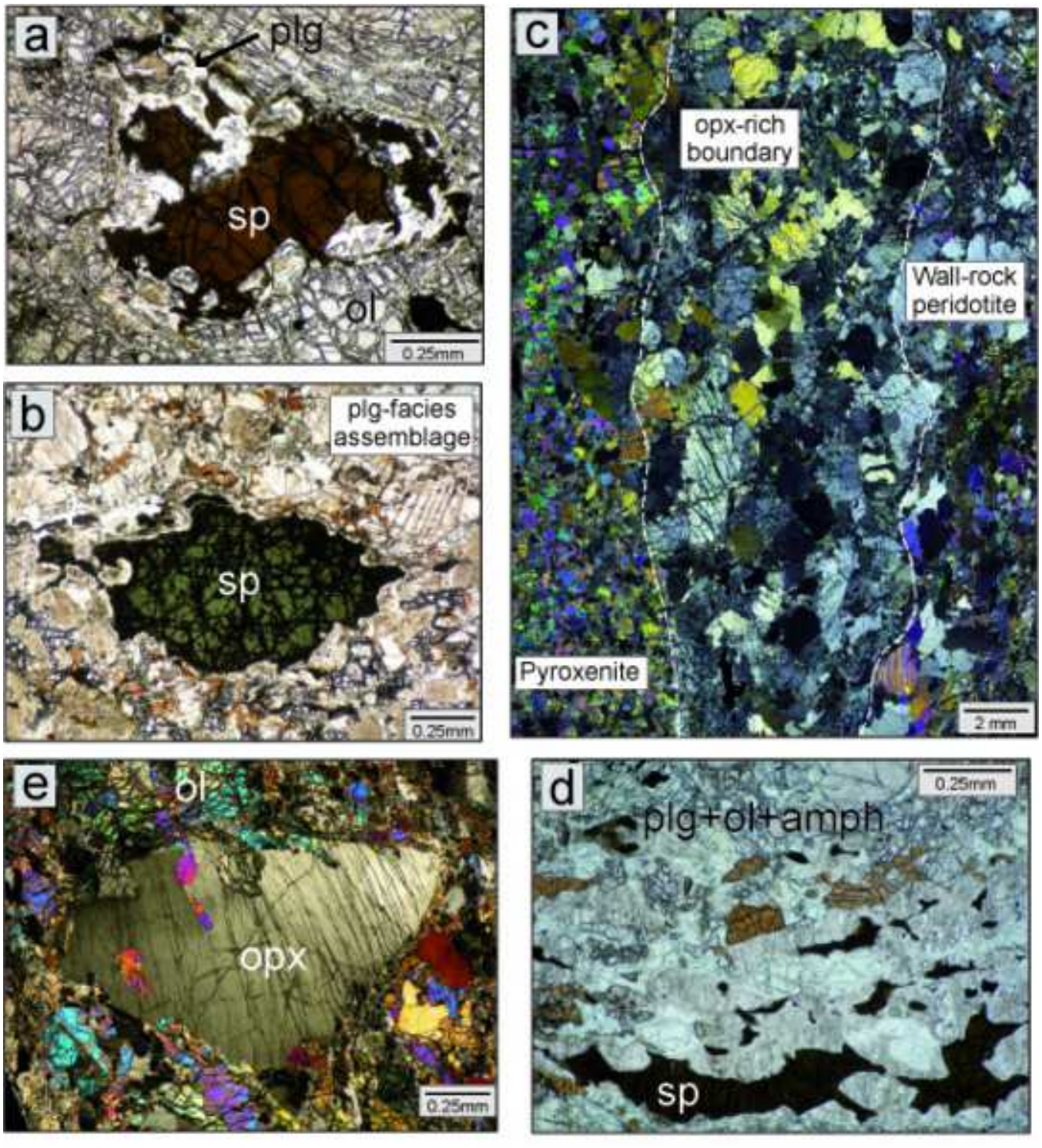

Figure 2

Figure3

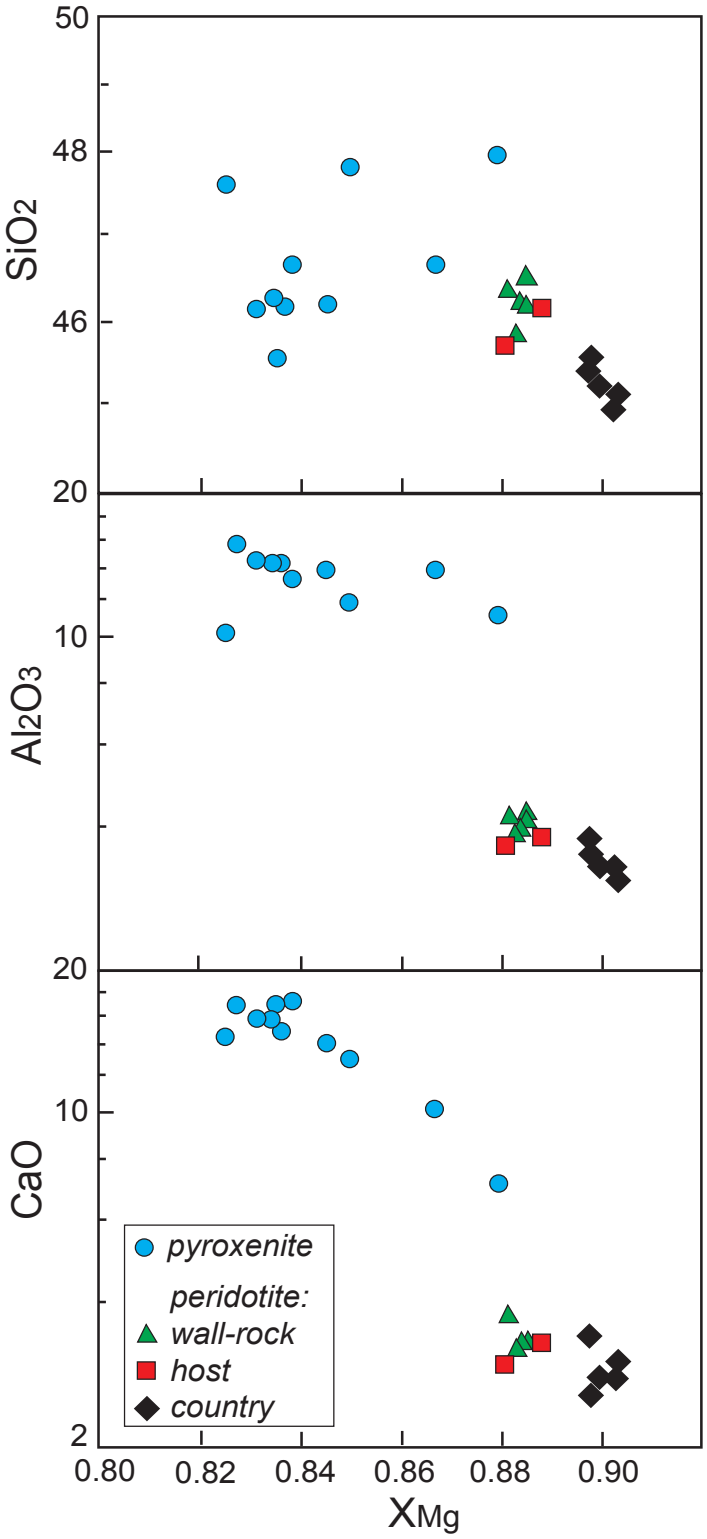

Figure 3

Figure4

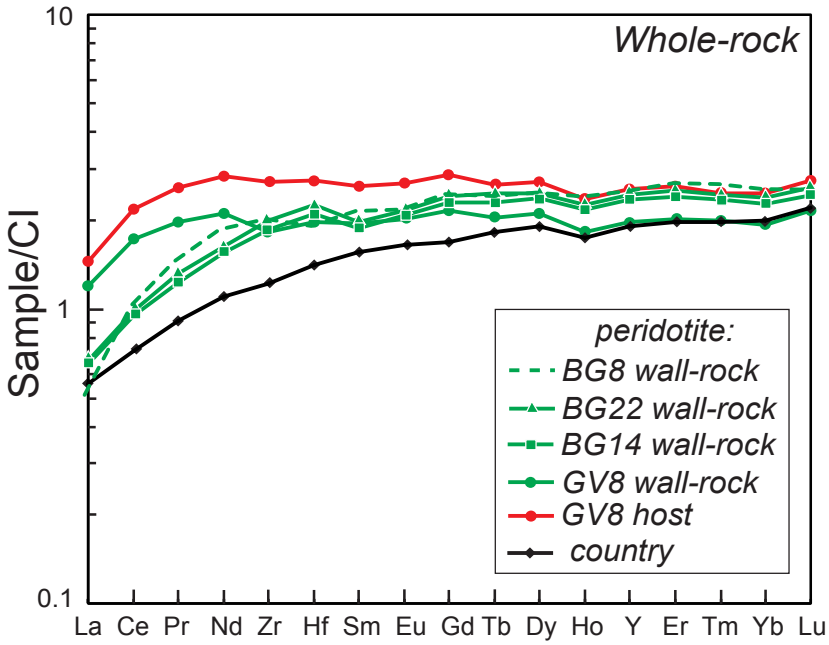

Figure 4

Figure5

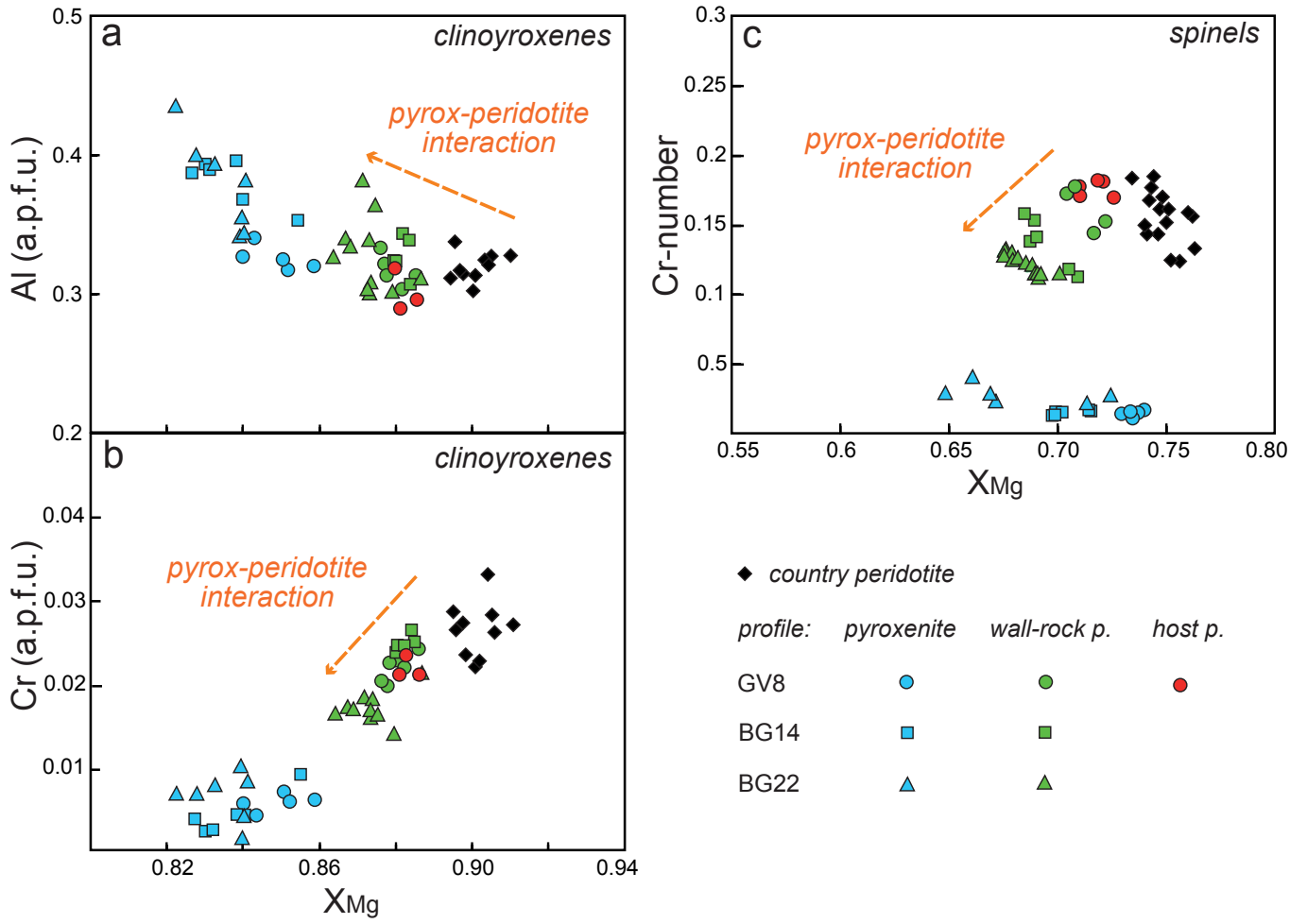

Figure 5

Figure6

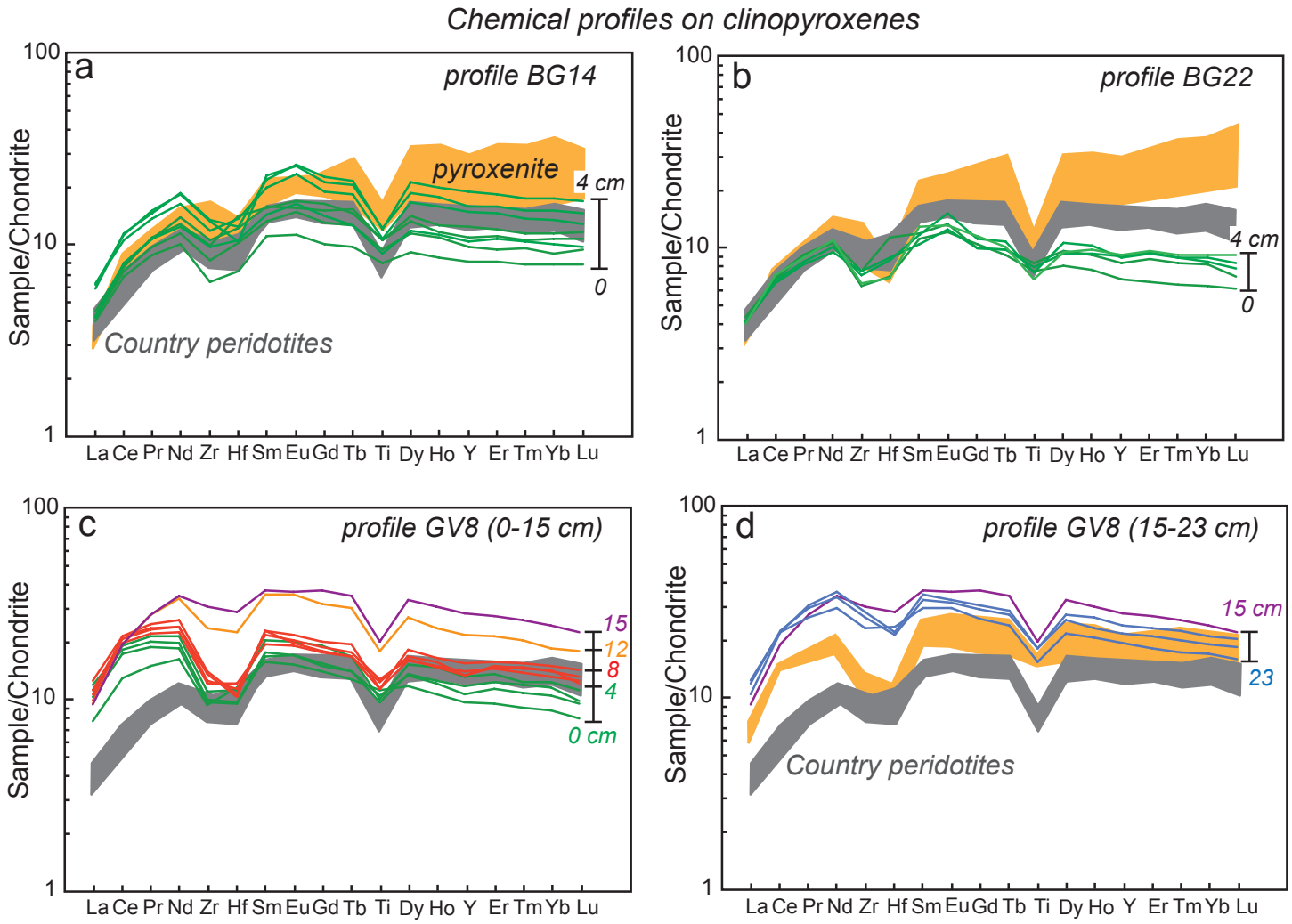

Figure 6

Figure7

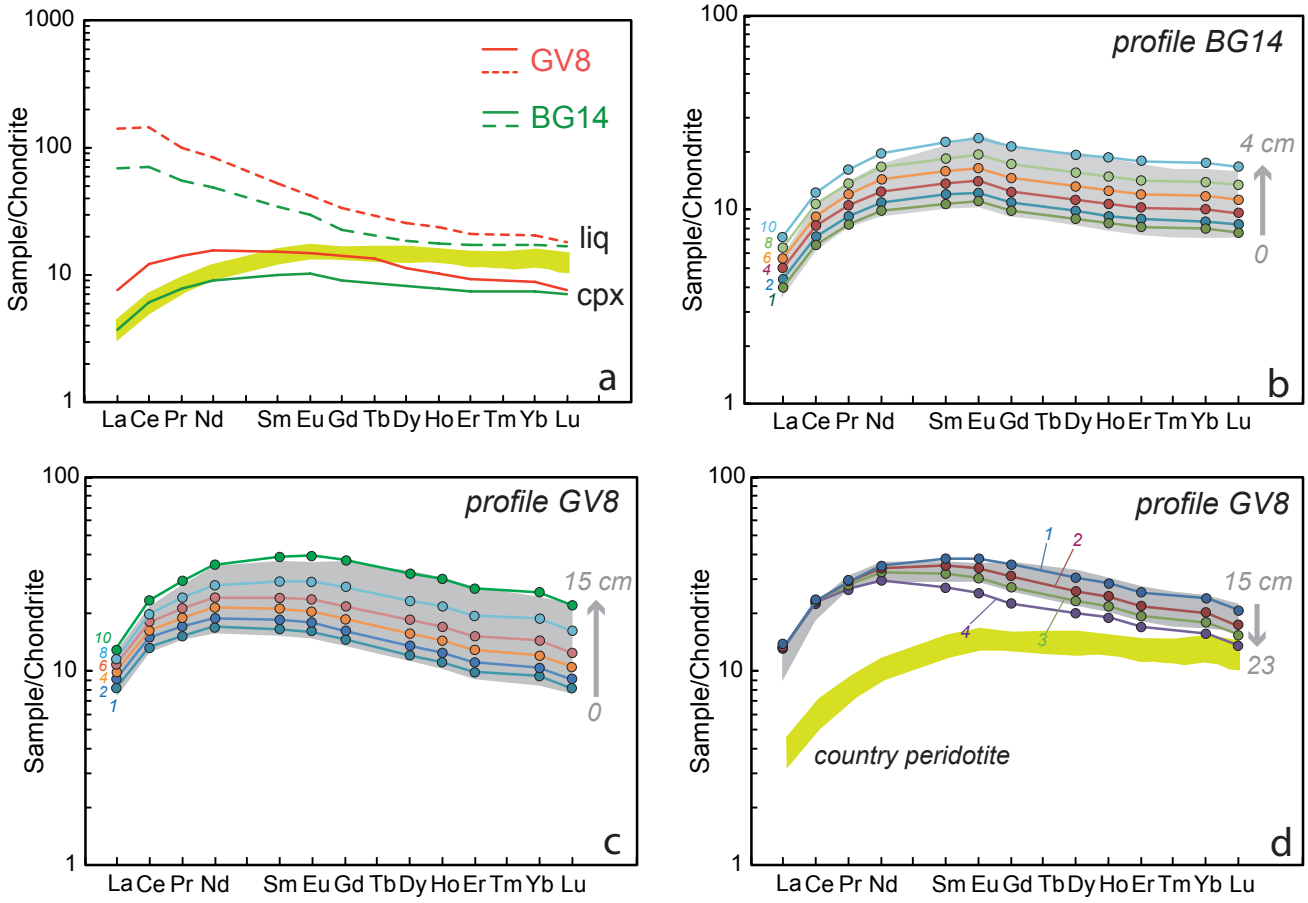

Figure 7

Figure8

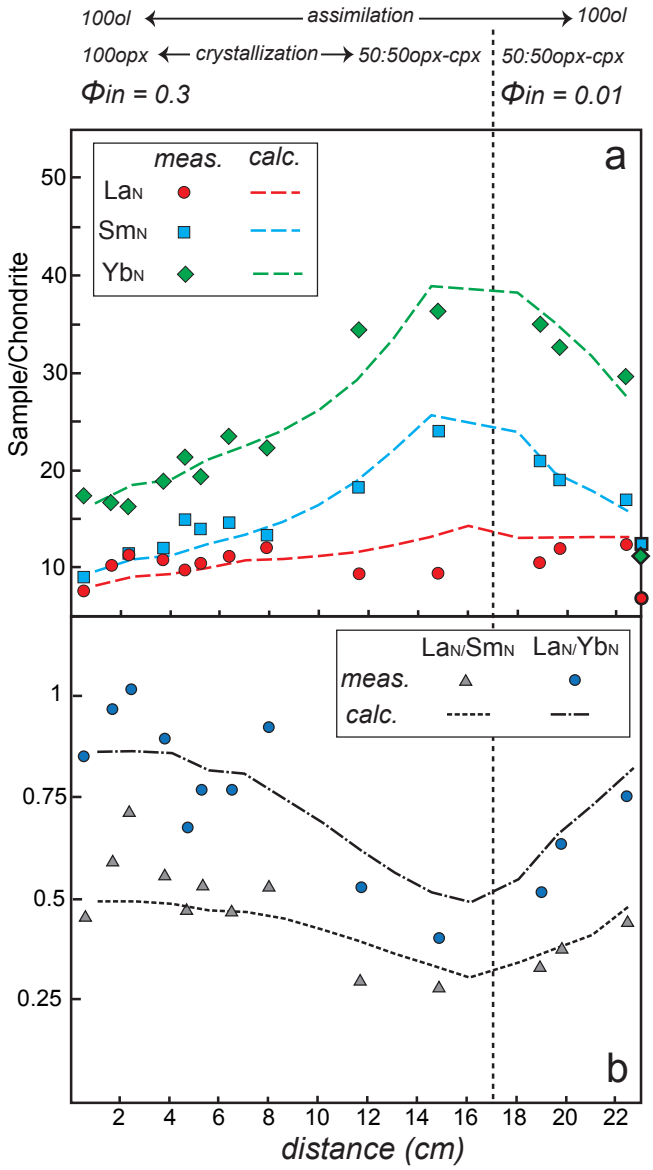

Figure 8

Table1

Click here to download Table: Table 1.docx

Table 1

Whole-rock major and trace element compositions.

	Country-rock peridotites					BG8	BG13	BG3	*BG14 profile*		*BG22 profile*		*GV8 profile*		
Sample	BG1	BG6	GV18	ERS2/2	MC7	w-r	w-r	host	pyrox	w-r*	pyrox	w-r*	pyrox	w-r*	host*
SiO_2	42.23	42.11	41.94	42.43	41.13	43.57	42.72	42.07	43.62	43.41	44.38	43.60	46.46	42.82	42.96
TiO_2	0.13	0.11	0.11	0.11	0.14	0.18	0.15	0.15	0.34	0.15	0.35	0.16	0.45	0.16	0.19
Al_2O_3	3.15	3.17	3.25	3.58	2.96	4.02	3.72	3.51	13.86	4.03	12.75	3.94	11.50	3.46	3.69
Fe_2O_3	8.50	8.38	8.43	8.39	8.36	9.22	9.05	8.74	6.35	8.94	5.98	9.13	6.71	9.71	9.44
MnO	0.12	0.12	0.12	0.00	0.12	0.14	0.14	0.12	0.14	0.13	0.14	0.12	0.14	0.13	0.13
MgO	38.37	39.04	37.28	36.97	36.90	34.48	34.74	34.83	15.80	34.65	15.65	35.48	19.17	36.16	35.78
CaO	2.64	2.63	2.39	3.22	2.75	3.59	3.10	3.03	15.13	3.14	16.41	3.18	12.64	2.82	3.05
Na_2O	0.17	0.18	0.16	0.25	0.13	0.20	0.20	0.11	0.33	0.13	0.34	0.14	0.52	0.20	0.25
K_2O	0.00	0.01	0.01	0.00	0.00	0.05	0.03	0.01	0.28	0.03	0.18	0.04	0.07	0.02	0.02
P_2O_5	0.01	0.02	0.01	0.00	0.00	0.02	0.02	0.02	0.03	0.02	0.02	0.04	0.04	0.01	0.03
Cr_2O_3	0.30	0.29	0.36	0.41	0.35	0.26	0.31	0.30	0.13	0.32	0.12	0.31	0.17	0.30	0.31
LOI	5.03	4.89	6.01	4.66	7.16	3.95	5.27	6.29	4.98	5.04	4.66	5.12	3.13	4.54	4.08
Tot.	100.65	100.95	100.07	100.02	100.00	99.68	99.44	99.18	101.00	99.99	100.98	101.26	100.99	100.32	99.93
Mg#	0.90	0.90	0.90	0.90	0.90				0.83	0.88	0.84	0.89	0.85	0.88	0.88
Sr	22	10	14.9	12.2	9	41	---	---	602	75	491	35	274	15	17
Y	3.3	3.1	2.73	---	3.2	3.7	---	---	11.8	3.54	12.5	3.59	8.2	2.85	3.68
Zr	---	---	4.83	---	---	---	---	---	18	7.85	20	7.82	19	7.24	11
La	---	---	0.130	---	---	---	---	---	0.34	0.156	0.38	0.161	0.87	0.280	0.339
Ce	0.59	0.36	0.435	0.56	0.42	0.61	---	---	1.39	0.593	1.53	0.607	2.6	1.041	1.317
Pr	0.11	0.08	0.082	0.10	0.09	0.13	---	---	0.28	0.117	0.31	0.117	0.39	0.176	0.230
Nd	0.66	0.54	0.499	0.60	0.60	0.85	---	---	1.84	0.742	2.1	0.747	2.1	0.953	1.276
Sm	0.28	0.24	0.229	0.27	0.27	0.32	---	---	0.78	0.290	0.86	0.293	0.83	0.286	0.385
Eu	0.11	0.10	0.092	0.12	0.11	0.12	---	---	0.357	0.121	0.394	0.124	0.352	0.113	0.150
Gd	0.41	0.36	0.332	0.41	0.40	0.48	---	---	1.54	0.475	1.66	0.479	1.22	0.424	0.559
Tb	0.08	0.07	0.066	0.08	0.08	0.09	---	---	0.29	0.090	0.31	0.089	0.23	0.074	0.096
Dy	0.51	0.47	0.465	0.58	0.50	0.61	---	---	1.93	0.601	2.05	0.617	1.48	0.513	0.658
Ho	---	---	0.106	---	---	---	---	---	0.42	0.136	0.45	0.139	0.3	0.110	0.141
Er	0.34	0.32	0.312	0.39	0.35	0.43	---	---	1.32	0.400	1.4	0.407	0.91	0.320	0.415
Tm	0.05	0.05	0.048	0.06	0.05	0.07	---	---	0.205	0.059	0.213	0.061	0.137	0.048	0.060
Yb	0.37	0.33	0.323	0.38	0.34	0.42	---	---	1.35	0.387	1.41	0.395	0.88	0.314	0.400
Lu	0.05	0.05	0.054	0.06	0.05	0.06	---	---	0.208	0.063	0.223	0.063	0.141	0.053	0.066
Hf	0.20	0.20	0.147	0.20	0.20	0.20	---	---	0.4	0.235	0.5	0.231	0.5	0.205	0.285
Sc	13	13	13	---	13	14	---	---	39	12	39	12	31	11	13
V	58	51	---	---	70	87	---	---	182	77	195	76	191	68	78

Whole-rock analyses were performed by lithium metaborate/tetraborate fusion ICP techniques at the Actlabs Laboratories.

(Western Ontario, Canada; http://www.actlabs.com).

(*) Trace element analyzed on a quadrupole VG-PQ2 ICP-MS at University of Montpellier (France).

Major elements compositions are in wt.%; trace elements contents are in ppm.

All major element analyses are from Borghini et al. (2013), except for sample GV18.

Data of pyroxenites are from Borghini et al. (2016).

Table2

Click here to download Table: Table 2.docx

Table 2

Trace element compositions of clinopyroxene porphyroclasts from selected pyroxenite-peridotite profiles.

Sample	ERS2/2		BG6	GV18		BG14 pyroxenite			BG14 Wall rock							
*dfP**	*Country peridotites*					---§	---§	---	*0.2*	*1.1*	*1.7*	*2.2*	*2.5*	*3.4*	*3.7*	*3.8*
Sr	19	9.0	7.6	15	8.1	7.2	5.7	3.1	34	15	24	18	14	15	25	17
Y	19	21	23	19	22	36	21	39	12	16	14	15	18	27	21	23
Ti	3149	3920	3532	2953	3749	8678	6877	8587	3224	4286	3778	5469	6420	4879	6534	7410
Zr	30	38	41	31	40	47	31	55	23	36	30	36	39	49	43	49
La	1.1	0.91	0.76	0.87	0.79	0.58	0.59	0.59	0.87	0.92	0.90	0.90	1.0	1.3	1.4	1.3
Ce	4.2	4.1	3.1	4.3	4.4	3.9	3.9	3.7	3.8	4.3	4.0	4.4	4.4	6.4	5.9	6.3
Pr	0.77	0.74	0.67	0.83	0.87	0.82	0.78	0.82	0.73	0.90	0.81	0.89	0.88	1.2	1.1	1.3
Nd	4.5	4.4	4.3	4.9	5.4	5.7	5.1	5.8	4.2	5.3	4.8	5.2	5.8	7.8	6.8	7.7
Sm	1.9	2.0	2.1	2.1	2.4	2.8	2.2	2.6	1.5	2.1	1.8	2.0	2.2	3.0	2.7	3.1
Eu	0.78	0.83	0.84	0.78	0.96	1.1	0.95	0.95	0.59	0.88	0.77	0.85	0.81	1.4	1.2	1.3
Gd	2.6	2.9	3.0	2.7	3.3	3.9	3.2	4.1	1.8	3.0	2.4	2.6	2.7	4.1	3.4	3.9
Tb	0.46	0.54	0.61	0.50	0.60	0.85	0.53	0.88	0.33	0.49	0.42	0.42	0.51	0.72	0.61	0.69
Dy	3.0	3.5	4.0	3.3	4.1	6.2	3.8	6.9	2.1	3.0	2.6	2.7	3.2	4.7	3.7	4.2
Ho	0.71	0.77	0.90	0.74	0.90	1.36	0.82	1.60	0.44	0.60	0.56	0.58	0.65	1.02	0.82	0.91
Er	2.0	2.1	2.4	2.0	2.4	4.6	2.5	4.5	1.2	1.6	1.4	1.6	1.8	2.7	2.1	2.3
Tm	0.28	0.31	0.37	0.30	0.36	0.63	0.33	0.57	0.18	0.24	0.21	0.23	0.26	0.39	0.31	0.34
Yb	1.9	2.0	2.6	2.0	2.2	4.5	2.4	5.1	1.2	1.6	1.3	1.5	1.7	2.6	2.0	2.3
Lu	0.25	0.26	0.37	0.28	0.31	0.66	0.39	0.66	0.18	0.24	0.21	0.22	0.26	0.38	0.29	0.33
Hf	0.91	1.2	1.0	0.78	1.1	0.80	0.87	1.2	0.70	1.4	1.0	1.0	1.2	1.2	1.3	1.0
Sc	51	65	72	48	59	85	57	144	43	41	36	41	42	53	49	56
V	269	321	277	241	273	379	344	363	229	226	217	217	229	268	243	285

	GV8 pyroxenite			GV8 Wall rock					GV8 Host						
	---§	---§	---§	*0.3*	*1.6*	*2.3*	*3.7*	*4.6*	*5.2*	*6.4*	*7.8*	*11.6*	*14.8*	*18.9*	*19.7*	*22.4*
Sr	7.8	8.1	7.4	26	17	33	23	14	16	16	20	17	11	16	15	14
Y	23	29	31	15	17	18	20	21	21	24	21	32	43	37	34	30
Ti	6529	7002	6796	4830	4532	4144	4320	5447	5299	4918	4868	7671	8622	7985	7936	6725
Zr	42	52	51	36	37	39	43	49	47	53	54	92	117	112	103	91
La	1.5	1.7	1.7	1.8	2.4	2.8	2.6	2.3	2.5	2.6	2.9	2.2	2.2	2.5	2.8	2.9
Ce	8.5	8.6	8.6	7.6	10.3	10.8	11.4	12.7	11.7	12.3	12.8	11.5	11.5	13.4	13.5	13.3
Pr	1.5	1.6	1.4	1.3	1.7	1.7	1.9	2.1	1.9	2.0	2.2	2.4	2.4	2.7	2.6	2.4
Nd	8.0	9.1	7.7	7.2	8.2	8.7	9.6	11	10	11	12	15	15	16	15	13
Sm	3.4	3.6	2.7	2.3	2.5	2.6	3.0	3.1	2.8	3.3	3.3	5.1	5.3	5.1	4.8	4.4
Eu	1.0	1.2	1.4	0.84	0.95	0.94	1.1	1.1	1.1	1.2	1.1	1.9	2.0	1.8	1.8	1.7
Gd	3.4	4.3	4.7	2.7	3.0	2.9	3.7	3.6	3.4	3.9	3.5	6.1	7.1	6.0	5.7	5.1
Tb	0.61	0.79	0.85	0.46	0.51	0.50	0.60	0.63	0.60	0.69	0.60	1.07	1.24	1.05	0.985	0.87
Dy	3.8	5.4	5.5	2.8	3.2	3.2	3.6	3.9	4.0	4.3	3.8	6.4	8.0	6.6	6.2	5.3
Ho	0.85	1.20	1.24	0.58	0.67	0.69	0.81	0.81	0.86	0.91	0.82	1.29	1.66	1.46	1.29	1.15
Er	2.4	3.2	3.4	1.5	1.8	1.9	2.1	2.3	2.4	2.5	2.3	3.4	4.3	3.7	3.4	2.9
Tm	0.36	0.48	0.52	0.22	0.26	0.29	0.29	0.35	0.34	0.37	0.33	0.49	0.61	0.54	0.48	0.42
Yb	2.7	3.2	3.2	1.4	1.7	1.9	2.0	2.2	2.3	2.4	2.1	3.0	3.9	3.4	3.1	2.8
Lu	0.35	0.43	0.49	0.19	0.23	0.24	0.27	0.32	0.29	0.34	0.30	0.43	0.53	0.49	0.45	0.39
Hf	1.2	1.2	0.89	1.2	1.0	1.0	1.2	1.2	1.3	1.1	1.1	2.3	2.9	2.3	2.2	2.5
Sc	48	56	78	49	45	47	50	49	52	54	54	52	63	63	62	64
V	376	322	353	251	246	245	256	276	279	268	272	310	340	313	327	304

Contents are in ppm.

dfP = distance from pyroxenite-peridotite contact (cm).*

(§) data from Borghini et al. (2016)

Supplementary Figure 1

Click here to download Background dataset for online publication only: Suppl.Fig.1.pdf

Supplementary tables

Click here to download Background dataset for online publication only: Suppl_tables_rev.xls